Chemical Engineering Science 281 (2023) 119202

Contents lists available at ScienceDirect

Chemical Engineering Science

journal homepage: www.elsevier.com/locate/ces

Multi-period optimization for the design and operation of a flexible power-to-methanol process

Andrea Maggi [a], Jens Bremer [b], Kai Sundmacher [a,c,*]

[a] Max Planck Institute for Dynamics of Complex Technical Systems, Sandtorstraße 1, 39106 Magdeburg, Germany
[b] Clausthal University of Technology, Institute of Chemical and Electrochemical Process Engineering, Leibnizstraße 17, 38678 Clausthal-Zellerfeld, Germany
[c] Otto von Guericke University Magdeburg, Universitätsplatz 2, 39106 Magdeburg, Germany

ARTICLE INFO

Keywords:
Methanol
Multi-period optimization
Flexibility

ABSTRACT

The increasing share of renewable resources in the context of energy transition scenarios requires new methodologies for the design and operation of chemical production facilities, which must adapt to the unsteady nature of their power supply. In this contribution, a highly flexible, fully electrified Power-to-Methanol process, supplied with unsteady wind power generated within the system boundaries, is designed by means of a large-scale NLP multi-period optimization for profit maximization. The problem is constrained by detailed models of interconnected units, feasibility conditions, and discretized power loads (periods) associated with their probability of occurrence. External power must be integrated into the plant to sustain feasible operations when the renewable input is not sufficiently available. Results show that the price at which the external power is purchased determines whether the resulting flexible-plant configuration is competitive with a comparable plant, optimized for steady-state operations ensured by large hydrogen or electricity buffers. Intermediate configurations represented by small buffers and semi-flexible operations constitute an important compromise for future applications of this novel approach.

1. Introduction

The production of green hydrogen from renewable power and its conversion into chemicals by means of water electrolysis and chemical processes (Power-to-X, or P2X) is highly relevant to energy transition scenarios all over the world. Design and operation of such process systems must take into account the unsteady nature of the power supply (load) in the medium and short term. To ensure a continuous and temporally stable supply of target products to the market, the intermittency of natural resources, such as wind and solar, should be dampened by buffering devices. Alternatively, Power-to-X is designed and run flexibly to convert the renewable power input into valuable chemical products.

As shown in Fig. 1, buffering strategies can be implemented along the production path for the conversion of water and a carbon source into a generic valuable chemical component, X. In case B.I, a buffer for the storage of electricity is used before any chemical conversion process; in case B.II, hydrogen is stored after water electrolysis and before the chemical synthesis. The exact allocation of the buffering device along the process coordinate determines the extent of flexibility of the plant, i.e., the plant section which follows the buffer operates in steady state. Consequently, for case F where no buffers are involved, the Power-to-X process is operated flexibly. The implication of different buffering scenarios on process operations has been recently reviewed in a relevant contribution by Mucci et al. (2023). In addition, this work reports that only a few studies consider the optimization of highly integrated processes connecting different unit operations. In this context, process flexibility introduces new challenges in the operation and design of the systems.

Typical optimization techniques for the design of chemical plants with detailed models determine the size of process units for a single, nominal load. Nevertheless, there is no guarantee that the identified design is the best solution for loads other than nominal. Instead, dedicated optimization strategies should be implemented to account for flexible plant operations, where a detailed description of process units, interconnections and operating windows is incorporated. Furthermore, Bruns et al. (2020) reported on the definition and use in literature of the term flexibility, which has become increasingly important in the context of production processes in recent years, but lacks a comprehensive categorization. Their conclusions highlighted that, although an enormous methodological development has been attained, literature still lacks the

* Corresponding author at: Max Planck Institute for Dynamics of Complex Technical Systems, Sandtorstraße 1, 39106 Magdeburg, Germany.
E-mail address: sundmacher@mpi-magdeburg.mpg.de (K. Sundmacher).

https://doi.org/10.1016/j.ces.2023.119202
Received 29 April 2023; Received in revised form 8 August 2023; Accepted 17 August 2023
Available online 23 August 2023

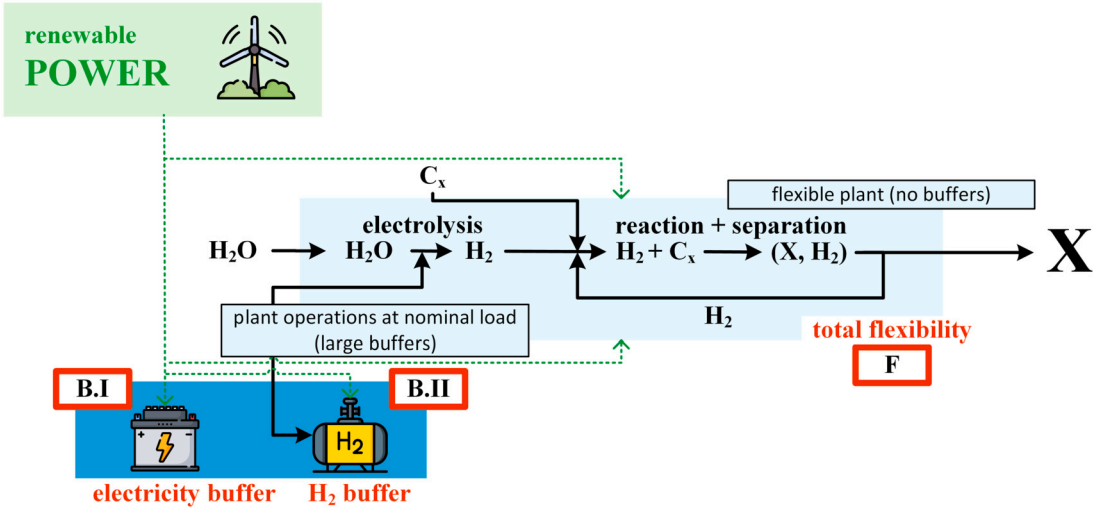

Fig. 1. Buffering strategies for a generic P2X process determine the extent of process flexibility involved. Electricity and hydrogen buffering strategies are denoted with B.I and B.II, respectively (plant design and operations at a single, nominal load). Alternatively, the whole process can be operated flexibly (strategy F).

applications to complex and more realistic problems. Instead, it mainly focuses on quasi-convex feasibility domains, often far from a reasonable description of real production processes.

Grossmann and Sargent (1978) defined a problem class for plant design under uncertainty, where the probability of occurrence is associated with a given set of values of the uncertain parameters. The final objective function is given by a finite sum of single entries, each weighted by the corresponding value of probability. The solution of the weighted objective function is then combined with the nominal design solution, i.e., at the nominal value of the uncertain parameters, to obtain over-design factors. Nevertheless, the applications are restricted to monotonic equations. The authors introduced an important distinction between design variables (optimization variables shared across different sets of uncertain parameters), and control variables (adjusted in light of the actual prevailing operating conditions).

Grossmann and his group proposed a mixed-integer linear programming approach (MILP) for the synthesis and design of utility systems based on a novel methodology denoted as multi-period design optimization, for multi-period plant operations (Iyer and Grossmann, 1998). In their case-study, capital and operating costs are minimized in a linear programming framework. In addition, the correlation between problem size and number of periods was reported. More recently, Martín (2016) proposed the application of multi-period MILP optimization to a renewables-to-methanol system, where the nonlinearity of detailed models is decoupled from the design under uncertainty of wind and solar farms. Surrogate models are incorporated into the final problem formulation, which accounts for actual patterns of wind and solar power supply. Furthermore, Peng et al. (2019) proposed the application of simplified nonlinear models for superstructure optimization under intermittency introduced by predefined time series of renewable power supply. The authors distinguished between operating and design variables, the former are replicated and the latter are shared across the periods. Operating feasibility was ensured by the maximum equipment size required for any scenario. This approach is appropriate if the system does not include a detailed model. For instance, a reactor volume too large for the input power flowrate could lead to unattainable velocities or temperature hot spots. In a multi-period optimization application for superstructure networks of heat exchangers, Short et al. (2016) highlighted the need to verify that design results shared among periods are always feasible. Once again, the authors decoupled detailed model evaluation from multi-period optimization by means of an iterative procedure. At each iteration of the optimization, the maximum achievable size of the unit is selected and its feasibility across periods is checked before proceeding to a new iteration (decoupled approach).

In the field of Power-to-Methane on a plant level, Grünewald et al. approached the problem of defining the thresholds of permitted electrical loads of the plant by simulating each unit operation separately (Herrmann et al., 2020). The intersection between resulting feasibility areas thus identified the overall operation span of the interconnected system. Although this approach defines unit sizes prior to simulation, it is a valid method for comparing the results of optimization-based studies in terms of operating ranges. In a significant contribution by Chen et al. on process flexibility exemplified by the methanol synthesis (Chen and Yang, 2021), the behavior of a complex and interconnected plant supplied with renewable power is linearized from the results of Aspen Plus simulations. For the flexible plant sections, i.e. the water electrolysis and the methanol synthesis loop, optimal oversized designs are identified in a LP optimization, so that the system is able to attain all possible loads encountered during its operations. This study conveys that a necessary but not sufficient condition for a competitive flexible process is that the cost of storing its intermediate or final product is lower than the cost of buffering its renewable power supply. This is the case for methanol synthesis. Liquid (raw) methanol can be stored comparatively inexpensively compared to hydrogen or electricity.

In general, the implementation of simplified unit models or decoupled approaches in multi-period optimization frameworks and, in general, in flexibility studies allow to identify optimal solutions that do not guarantee the feasibility of flexible operations in the plant and the interplay between design and operating conditions, such as states and flowrate of reactor feeds. More recently, Zimmermann et al. (2022) included a detailed reactor and catalyst particle model within a multi-period approach for synthetic natural gas generation. In this article, the authors maximized the space-time yield of the methanation reactor subject to variable feed loads provided by renewable hydrogen. Unlike previous works, a detailed nonlinear model of the methanation reactor was directly included in the framework of multi-period design optimization. Therefore, design, catalyst concept and operating strategies for the unit operation are optimized.

With the prospect of high electrification of the chemical industry and heavy use of unsteady power supply, more and more process units within the production cycle will be strongly interdependent. Power-to-X plants are subject to various types of uncertainties, not only due to the inherent fluctuations of local renewable resources, but also related with the volatility of electricity prices: good decision making needs to be supported by optimization under uncertainty (Burre et al., 2020; Zhang and Grossmann, 2016). As recommended by Dieterich et al. in their review on power-to-liquid technologies, the yet limited research on flexibility and dynamic synthesis should be extended to entire systems, where the

integration between individual units can show non-intuitive syngery effects, typical of these setups (Dieterich et al., 2020). Ideally, any spike in renewable electricity shall be absorbed within the plant, e.g., by electric heat exchangers, compressors, electrolyzers and electrified reactors for endothermic syntheses. The placement of buffering devices along the process coordinate determines both the extent of process flexibility and, consequently, the complexity in design and operations. Prabhakaran et al. recently contributed in this direction with their analysis of a dynamically operated three-phase methanation reactor, in the context of a decentralized energy network with power generation (solar panels, grid inputs), supply (households, grid outputs) and storage items (batteries and thermal storage) (Prabhakaran et al., 2023). The distributed dynamic model of a slurry methanation reactor, where the liquid phase was used to control the heat generation, is then plugged into a larger network model for the dynamic simulation of the whole system under fluctuating power supply, demonstrating the operability of their novel reactor concept. In this setting, batteries were just enough to cover for short-term storage, whereas grid inputs were required for longer periods of unavailable local electricity. Dynamic simulation approaches can also help identifying lower bounds to the feasible loads. A relevant example is found in the work by Kreitz et al. on Power-to-Methane (Kreitz et al., 2020), which stated that below 20% of the nominal load, the electrolyzer cannot be safely operated. The authors considered the sequence of an alkaline electrolyzer and a methanation reactor described by a distributed model. Furthermore, lower and upper thresholds to allowable loads for exothermic reactors are dictated by catalyst deactivation and uncontrolled hot spot temperatures (Moioli, 2022). However, this study did not account optimal design under fluctuating power supplies: the units were sized to ensure acceptable gas purities for the nominal, i.e., maximum load, scenario. This trend calls for an effort toward incorporating a detailed description of the full-scale plant in the context of a multi-period optimization set-up, yet to be found in the literature.

Methanol is a relevant key molecule in the chemical industry. Not only is it an important intermediate for further synthesis of chemicals, such as formaldehyde, acetic acid, and MTBE (Riaz et al., 2013), but it is also blended with gasoline in internal combustion engines as octane booster, or possibly in pure form, as reviewed in Verhelst et al. (2019). Methanol is produced industrially in large plants and cooled fixed-bed reactors. The conversion of carbon monoxide and carbon dioxide to methanol is moderately exothermic and proceeds with a decrease in the number of moles:

$$CO_2 + 3\,H_2 \rightleftharpoons CH_3OH + H_2O \qquad \Delta H_R(298\,K) = -53\,kJ\,mol^{-1} \qquad (1)$$

$$CO + 2\,H_2 \rightleftharpoons CH_3OH \qquad \Delta H_R(298\,K) = -95\,kJ\,mol^{-1}, \qquad (2)$$

$$CO_2 + H_2 \rightleftharpoons CO + H_2O \qquad \Delta H_R(298\,K) = \;\;42\,kJ\,mol^{-1}, \qquad (3)$$

favored by high pressure and low temperature. In parallel, the reverse water-gas shift reaction contributes to the generation of carbon monoxide. Established technologies adopt fixed-/packed-bed reactors, typically on $CuO/ZnO/Al_2O_3$, cooled by boiling steam at a suitable pressure (Dieterich et al., 2020). An example is the first-stage of the Lurgi technology. Although these systems benefit from the economy of scale, decentralized plants that take advantage of locally generated renewable power may be limited in terms of the available area for the installation of wind or solar power plants. Furthermore, methanol can be easily buffered to a liquid state at room temperature, provided that a flexible process is admissible. Flexibility can limit the cost of intermediate buffering devices. Therefore, fast system loading scenarios have been the subject of recent simulation-based investigations, where swings from 10% to 100% have been successfully attained (Dieterich et al., 2020).

In this contribution, a multi-period optimization approach aims at simultaneously identifying optimal design and operation strategies for a highly electrified, small-capacity Power-to-Methanol plant for a discrete number of power inputs (load levels). Thermal duties are entirely

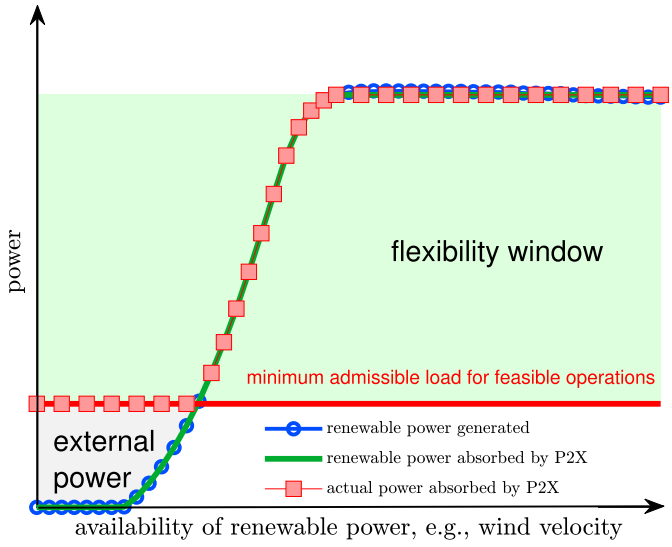

Fig. 2. Flexibility window for maximum plant flexibility. The renewable power generated at low wind velocities does not guarantee feasible plant operations, which are ensured via integration of external grid electricity.

satisfied by the electrical inputs, e.g., electrical heat exchangers, which substitute traditional thermal processes. Water is converted into hydrogen in an electrolyzer at high power demand, and carbon dioxide into carbon monoxide via reverse water-gas shift. Renewable power is assumed to be generated from a local wind park owned by the chemical company. The renewable energy generated locally is used exclusively to support the requirements of the methanol plant, as the injection of surplus electricity into the power grid must be avoided. This is motivated by the need to exploit peaks in cheap locally renewable power, then easily stored into a valuable product. At any given time, the available power must be optimally distributed among the unit operations within the process, which constitutes a non-trivial decision task. Methanol and water are collected comparatively inexpensively in liquid form and buffered (Chen and Yang, 2021), so that their separation can be conducted in steady-state, unlike the entire upstream section of the plant, which may be operated flexibly. This approach is identified in strategy F (Fig. 1), which involves the highest process flexibility. Reactor size and active area of electrolysis (design), feed policies, bypass and recycle ratios, discharge pressures from compression stages, and coolant temperature for the methanol reaction (operations) are optimized to attain the maximum profit. The extent of attainable flexibility for this process is defined by the lowest threshold of the power supplied by the renewable power plant, below which the methanol plant cannot be operated.

This suggests two possible operation strategies:

1. cyclic and frequent plant shutdowns at loads below the threshold;
2. purchase of external power at reasonable negotiated prices.

In this study, strategy 1. is not considered. It is economically unattractive due to loss of production, and is technically demanding as it implies that frequent and rapid shutdowns of reactors, compressors and electrolyzers are feasible. In contrast, strategy 2. for maximum plant flexibility (F) shall be benchmarked with the extreme case of large buffers for electricity or hydrogen (buffering case B.I and B.II), and steady-state operations at a nominal load unvaried throughout the year, respectively.

Fig. 2 is a graphical representation of operation strategy 2. The power generated by the renewable resource (blue curve) is entirely absorbed by the chemical plant. Therefore, the renewable power supplied to the process (green curve) coincides with the generated renewable power. Nevertheless, the minimum admissible load for feasible oper-

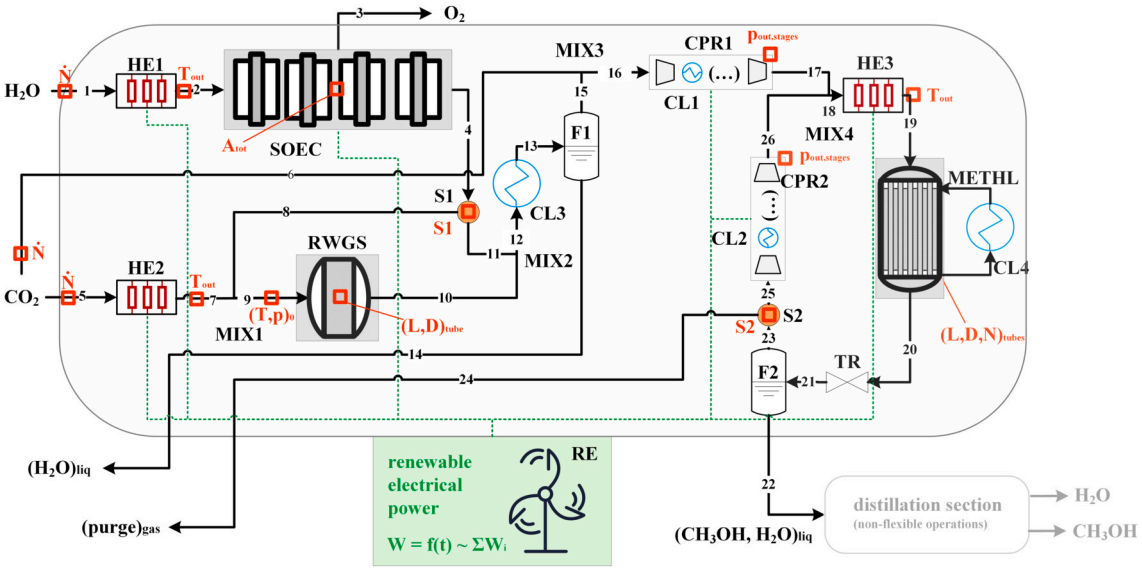

Fig. 3. Overall plant layout for the generation of a binary mixture of methanol and water. The final distillation section is not highlighted, as it operates independently of the unsteady power supply. Feedstock water and carbon dioxide are not part of the optimization setup, but some options are evaluated separately after Section 7.1 dedicated to optimization results.

ations (red horizontal line) defines the lowest attainable power input to the process, which ensures feasible operations. For this reason, the curve representing the actual power supplied to the process (red markers) follows the trend of renewable power until it stabilizes at the minimum admissible load. This occurs when the natural resource is too scarce to attain the minimum power threshold without the external integration of grid electricity. In this case, the plant operates flexibly within the power range comprised within the flexibility window (green area).

In the following sections, the modeling equations, elaborated in appendix, are reported. Next, the objective functions, case-studies and final optimization problems are reported before a comparative discussion of the results and conclusions are presented.

2. Plant layout

2.1. Plant sections: production and separation

Methanol is generated in a production section, followed by its separation from water. Fig. 3 illustrates fine process details in terms of upstream and production, whereas the following distillation section is drafted as a simple input-output block. Distillation is preceded by flash separation of liquid water and methanol. An unsteady power supply – green box for renewable energy (RE) – is to be absorbed within the production section. Distillation relies on a nominal feed and steady energy supply ensured by electric batteries. In this study, it is assumed that the distillation unit cannot be operated flexibly (Chen and Yang, 2021). For this reason, its feed flowrate must be stabilized by means of a relatively inexpensive buffering device for the process stream (blender), placed after the liquid outflow from the methanol flash drum. Reboilers duty and reflux ratios are influenced by the feed composition, partially stabilized by the blender. All this considered, it is here assumed that the water-methanol liquid mixture separated within the flash preserves its composition over time. This assumption will be validated against computational results and recalled in a later section of this article. The distillation section, unvaried across scenarios in terms of energy consumption and flowrate processed, shall not be accounted for in the modeling and formulation of the optimization problems, as the present study focuses on the comparison between buffering and flexible operations strategies. Since the design of a distillation sequence is not included in this study, it is also assumed that the liquid feed to the distillation unit does not contain dissolved supercritical gases. However, distillation calculations based on a shortcut model allow to estimate the thermal duty requirements, as reported in the discussion section (Section 7.2).

The Power-to-Methanol plant relies solely on electricity, also to supply heat to process flows and conversion processes. For this purpose, electrical heat exchangers (HE) are implemented.

2.2. Description of the process layout

Fig. 3 reports the process flow diagram, described in this section. A stream of deionized-desalinized water (stream 1) is vaporized and heated within HE1 up to the requirements of a SOEC (solid oxide high-temperature steam electrolyzer), selected due to its high power-to-hydrogen efficiency and flexibility (Buttler and Spliethoff, 2018; Dieterich et al., 2020), which generates oxygen at the anode (stream 3) and a mixture of water and hydrogen at the cathode (stream 4). A feed stream of carbon dioxide (stream 5) is heated in HE2. Its outlet stream 7 combines with stream 8 in mixer MIX1 (cathode outlets from SOEC) into stream 9 which feeds an adiabatic, single-staged reverse water-gas shift reactor (RWGS). Stream 8 is downstream of splitter S1, which allows to direct stream 4, a mixture of hydrogen and water, either to RWGS (stream 8) or to the methanol loop (stream 11). As a consequence, if stream 11 is selected, and the bypass stream of carbon dioxide (stream 6) is selected over stream 5 (makeup carbon dioxide to RWGS), RWGS is bypassed and the methanol loop is fed exclusively with water, hydrogen and carbon dioxide after mixing. Stream 6 is fed directly to a compressor train CPR1, after the mixing with stream 15 in MIX3, vapor head of a knockout drum F1: water, formed in RWGS and possibly unconverted in SOEC, has to be removed before compression CPR1. Thus, stream 12, composed from stream 11 and stream 10 after mixing MIX2, is cooled in CL3 and subsequently flashed in F1. Five adiabatic compression stages per compressor are assumed and represented compactly by the dashed boxes CPR1 and CPR2 in Fig. 3, which additionally include CL1 and CL2 and represent the intermediate coolers, three for each compressor group. Finally, outlet stream 17 feeds the methanol loop at mixer MIX4. Stream 18 is heated in HE3 to the required feed temperature in the multitubular, boiling-water cooled methanol reactor (METHL). Cooler CL4 cools the steam to its boiling point before recirculating in the reactor shell-side. The hot stream 20 is throttled (TR) and flashed in F2, which separates a cold liquid stream of water and methanol stream 22 from the gas stream 23, optionally purged by split-

ter S2 into stream 24, whereas stream 25 is recompressed in CPR2, then recycled as stream 26.

In Fig. 3, process degrees of freedom are illustrated in red and denoted with small squares on the flowsheet. They can be sorted into design and operating decision variables. Variables such as the area of SOEC stacks, number of reactor tubes, as well as tube length, diameter and catalyst diameter are design decisions. Operating decisions are: flowrates of feed streams to the entire plant, i.e., stream 1 (water), 5 and 6 (carbon dioxide), the feed states of the reactors, outlet states of the compressor stages, the (electric) heat exchangers, the discharge pressure of the throttling valve, the extent of purge from splitter S2 in the methanol loop and the extent of bypass of RWGS via splitter S1.

2.3. Water and carbon dioxide

This study on Power-to-Methanol focuses on the assessment of the production section independent of the source of H_2O and CO_2, which does not contribute to the results of the multi-period design optimization. However, this section provides a brief overview of the energy requirements for the prevailing technologies, seawater desalination and carbon capture, which are elaborated and adapted to this context after the discussion of the optimization results.

Section 2.2 reports on the need for a preconditioned feed stream of water to SOEC. Simoes et al. (2021) examined the energy demands of different water purification technologies. Seawater offers an unlimited water supply, although its salinity (about 3.5%) imposes the installation of a desalination device (reverse osmosis, RO). Its energy requirement is the highest among the purification technologies reviewed ($3\text{-}6\,\mathrm{kWh\,m^{-3}_{seawater}}$), and seawater losses occurring along the process reach up to 40%. A flexible desalter may be assumed, which thus follows the fluctuations in the renewable power. A fast flexible responses to a fluctuating electricity supply can be ensured by these systems, as reported by Ghobeity and Mitsos (2010). In their paper, the optimal operation of an oversized RO desalinator was attained by a global optimization approach. Alternatively, nominal, yearly-averaged operations can be ensured by means of batteries, similar to what has been assumed for the distillation unit in Section 2.1.

Green (direct air-capture, DAC) or blue (carbon capture from fluegas, CC) carbon dioxide can be provided to the process. A large number of technologies for DAC and CC are available at different development stages (Bui et al., 2018; Wang and Song, 2020). Aqueous amine scrubbing, e.g., MEA, is the established industrial solution for CC, although it requires a high regeneration energy. Respectively, reported temperature and thermal duty ranges at the reboiler are $100-125\,^{\circ}\mathrm{C}$ (Li et al., 2016), attractive for the heat integration, and $1000-1083\,\mathrm{kWh\,ton^{-1}_{CO_2}}$ (Li et al., 2016; Knudsen et al., 2009). Liquid sorbents for DAC (L-DAC) are potassium or sodium hydroxide, regenerated at high temperatures ($900\,^{\circ}\mathrm{C}$, as in Ozkan et al. (2022)), rather unattractive with respect to heat integration. On the contrary, solid sorbent DAC (S-DAC), a technology based on temperature-vacuum swing adsorption, requires lower typical regeneration temperatures, in the range $100-130\,^{\circ}\mathrm{C}$ (Ozkan et al., 2022), possibly heat-integrated with the cooling water of the methanol synthesis reactor. Reasonable values of electrical and thermal energy consumption consistent with current large-scale implementations of S-DAC are 640 and $2000\,\mathrm{kWh\,ton^{-1}_{CO_2}}$ (IEA, 2022; Ozkan et al., 2022).

3. Power supply and optimization setups

The available total electric power $\dot{W}_{\mathrm{tot}}$ is completely absorbed by the methanol plant and distributed according to the following constraint:

$$0 = \dot{W}_{\mathrm{tot}}(v_{\mathrm{wind}}) - \sum_{i \in I} \dot{W}_i(v_{\mathrm{wind}}), \qquad \text{(AE.Wtot)}$$

where set I includes all power sinks within the upstream-reacting section of the plant, represented in Fig. 3. The power requirements for the supply of feedstocks and for distillation operations are not included in $\dot{W}_{\mathrm{tot}}(v_{\mathrm{wind}})$, therefore the actual total power requirement and size of the wind farm would be scaled up according to these contributions (reference to Section 2.1). Wind velocity constitutes a yearly time-series. Therefore, its time dependency can be expressed as $v_{\mathrm{wind}} = v_{\mathrm{wind}}(t)$. Consequently, the total power absorbed by the methanol plant is a function of the wind velocity, $\dot{W}_{\mathrm{tot}}(v_{\mathrm{wind}})$, and time, $\dot{W}_{\mathrm{tot}}(t)$. The temporal dependency of the total power $\dot{W}_{\mathrm{tot}}(t)$ is not directly translated into dynamic models: for design purposes, dynamic transitions across periods do not need to be accounted for.

Wind velocities can be grouped into NP sub-domains, where the generic j-th sub-domain reads $\left(v_{\mathrm{wind},j-1}, v_{\mathrm{wind},j}\right]$ and is associated with a period, Π_j. Over the complete domain, the total power input is discretized as:

$$\dot{W}_{\mathrm{tot}}(v_{\mathrm{wind}}) = \begin{cases} \dot{W}_{\mathrm{tot},1} & \text{for } v_{\mathrm{wind}} \in \left[0, v_{\mathrm{wind},1}\right] \\ .. & \\ \dot{W}_{\mathrm{tot,NP}} & \text{for } v_{\mathrm{wind}} \in \left(v_{\mathrm{wind,NP}-1}, v_{\mathrm{wind,NP}}\right] \end{cases} \qquad (4)$$

The integration of the frequency distribution over a generic sub-domain $\left(v_{\mathrm{wind},j-1}, v_{\mathrm{wind},j}\right]$ provides the yearly probability of occurrence of period Π_j, and hence the yearly probability of occurrence of the total power, averaged for the current period, $\dot{W}_{\mathrm{tot},j}$. The probability of occurrence of period Π_j is denoted by ω_j.

In this Power-to-Methanol application, a Weibull distribution of wind velocities related with the power curve generated by a 50.5 MW wind park is assumed, supplied by 24 wind turbines of 2.1 MW (nominal output). Data for the power curve are retrieved from a technical sheet – see Appendix B.

The Weibull distribution is generated from a mean wind velocity and from a shape factor of 2, representing rather variable winds from a scale of 1 (highly variable winds) to 4 (highly stable winds). The mean wind velocity adopted to define the distribution is scaled from a value of $4.46\,\mathrm{m\,s^{-1}}$ at 10 m above the ground (Appendix B), to $8.9\,\mathrm{m\,s^{-1}}$ at 100 m, with a terrain rugosity factor of 0.3 (intermediate between the extreme values 0.2 and 0.4) applied to an exponential scaling rule: $v_{100\,\mathrm{m}} = v_{10\,\mathrm{m}}\,(100\,\mathrm{m}/10\,\mathrm{m})^{0.3}$. Details on the definition of the wind velocity frequency distribution can be found in Gualtieri and Secci (2012).

The first period is comprised between 0 and $6.45\,\mathrm{m\,s^{-1}}$, the latter value representing the mode of the Weibull distribution. In this first period, the power supplied by the wind park is not sufficient to ensure feasible plant operations. Therefore, power from an external source must be complementarily supplied to attain the minimum amount of power required. This power input of 12.625 MW, i.e., 25% of the maximum power supply provided by the wind park, is denoted by a red segment labeled as “integration” in Fig. 4. The last period is defined for the power output of 50.5 MW, which is the rated power output, i.e., maximum, of the wind park. The remaining periods are set between $6.45\text{-}8$, $8\text{-}10$ and $10\text{-}12\,\mathrm{m\,s^{-1}}$. Although this subdivision is arbitrary, it can provide a reasonable representation of the possible scenarios encountered during plant operations. The maximum number of periods is determined by the computational capacity of the machine on which the optimization is performed and by the problem size, as it scales with the number of periods.

3.1. Difference between design and operation variables

As discussed before, degrees of freedom labeled in red in Fig. 3 are grouped into two classes of variables: operating and design variables. Operation variables are function of the loads, i.e., they change between periods, whereas the plant design is determined once for all periods. Design variables are denoted by superscript (π). All degrees of freedom with their lower and upper bounds (LBX, UBX) are listed and described in Table 1. As an example, the optimizer identifies a single solution value for $D^{(\pi)}_{\mathrm{T,METHL}}$, the diameter of the methanol reactor tubes (design variable), while it identifies NP solutions (equal to the number of periods) for the cooling temperature T_{cool} (operation variable).

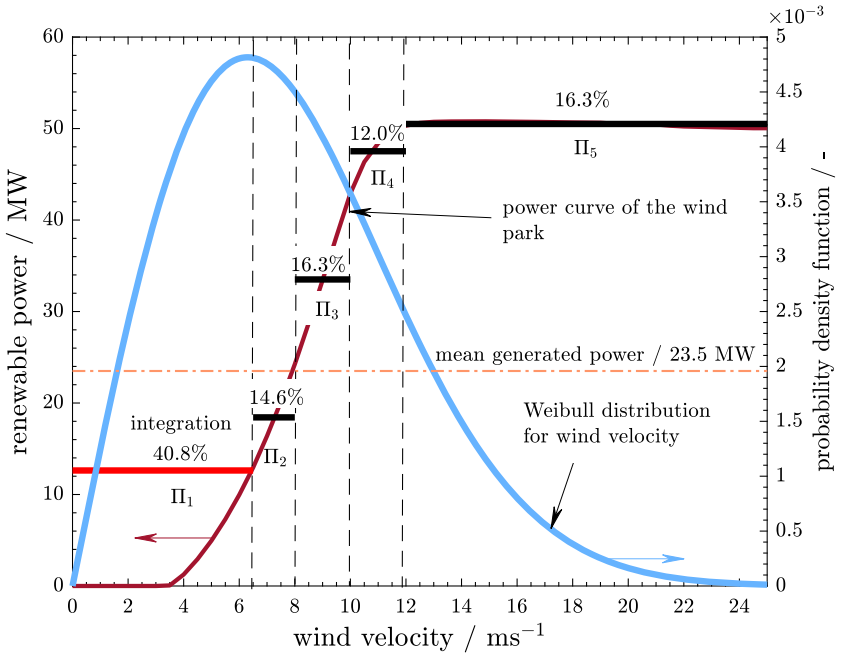

Fig. 4. Renewable power generated by the wind park as function of the wind velocity and probability density function. Periods are denoted by Π, and their probability of occurrence is given as a percentage value. Horizontal segments represent the mean power supply within a period. The integration of power from the grid required to ensure feasible operations for period Π_1 is indicated by the red segment. The dashed-dotted orange horizontal line represents the mean annual power generated (23.5 MW).

Table 1
List of relevant decision variables for design problems and related bounds. Variables shared among periods are denoted with superscript $^{(\pi)}$.

Variable	LBX	UBX	description	unit (SI)
$A^{(\pi)}_{\text{SOEC}}$	0.5	20000	total area SOEC	m^2
$L^{(\pi)}_{\text{T,RWGS}}$	0.1	2.1	tube length	m
$D^{(\pi)}_{\text{T,RWGS}}$	0.1	2.1	tube diameter	m
$N^{(\pi)}_{\text{T,METHL}}$	1	30000	number of tubes	–
$L^{(\pi)}_{\text{T,METHL}}$	1	15	tube length	m
$D^{(\pi)}_{\text{T,METHL}}$	0.02	0.15	tube diameter	m
$D^{(\pi)}_{\text{cat,METHL}}$	0	$1/10 D^{(\pi)}_{\text{T,METHL}}$	catalyst diameter	m
$\dot{N}_{\text{tot,1}}$	0	inf	H_2O, feed SOEC	mol s^{-1}
$\dot{N}_{\text{tot,5}}$	0	inf	CO_2, feed RWGS	mol s^{-1}
$\dot{N}_{\text{tot,6}}$	0	inf	CO_2, bypass RWGS	mol s^{-1}
$T_{\text{out,HE1}}$	1000	1300	feed temperature, SOEC	K
$T_{\text{out,HE2}}$	298	1010	feed temperature, RWGS	K
$T_{\text{out,HE3}}$	430	520	feed temperature, METHL	K
$\boldsymbol{p}_{\text{out(stage),CPR1}}$	1	100	vector of discharge pressures at each stage, CPR1	bar
$\boldsymbol{p}_{\text{out(stage),CPR2}}$	1	100	vector of discharge pressures at each stage, CPR2	bar
$p_{\text{in,SOEC}} \equiv p_{\text{in,RWGS}}$	1	5	pressure SOEC, RWGS (feed)	bar
$p_{\text{in,METHL}}$	20	100	feed pressure METHL	bar
T_{cool}	480	600	coolant temperature METHL	K
S1, S2	0	1	split factor: carbon dioxide to RWGS, purge	–

4. Mathematical models

The system is modeled by means of zero- and one-dimensional representations of the process units, interconnected by node balances. Ideal gas law is adopted in low pressure, high temperature operations, i.e., from the feedstock to stream 16 entering the first compression sequence CPR1. Elsewhere, non-ideal gas behavior is described through the Redlich Kwong Soave equation of state (RKS), i.e., in compressors CPR1, CPR2 and within the methanol loop. The assumption of equal interactions between different molecules (Lewis-Randal) allows the composition of the gas to be disregarded when evaluating compressibility factors. This approach has been adopted by Graaf (1986) for the methanol reactor at high temperatures. Mixing rules are added to the RKS equation of state to model units at high pressure and low temperatures: compressors CPR1 and CPR2, and the flash separator F2 within the methanol loop. Where Lewis-Randal applies, molar total concentrations for gas mixtures at high pressure are expressed as:

$$C_{\text{gas}} = \frac{p \sum_{\alpha \in S} \left(\frac{\zeta_\alpha}{Z_{\alpha,\text{gas}}} \right)}{R_{\text{gas}} T}. \tag{5}$$

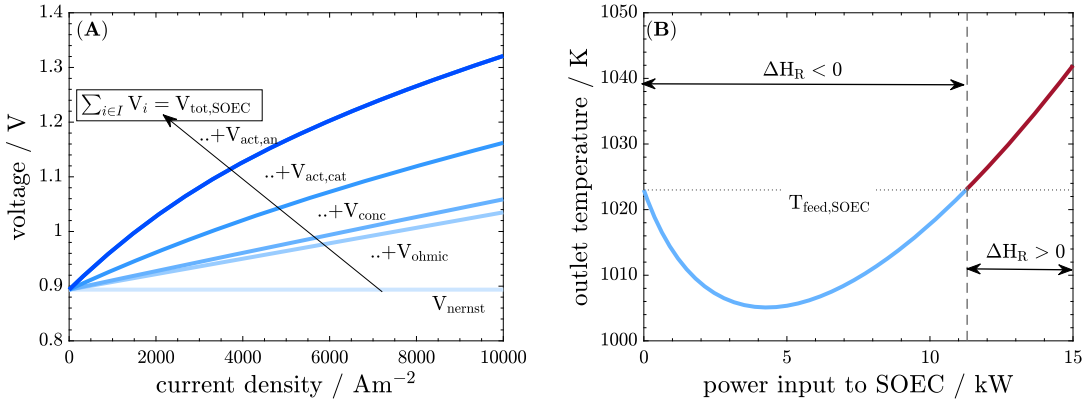

Fig. 5. (**A**) Cumulative definition of the polarization curves for the given cell parameters, as reported in Appendix C.1, from the ideal voltage (in the lightest blue) to the total voltage (in the darkest blue); (**B**) definition of the outlet temperature for a feed temperature of 1023 K, fixed cell parameters (Appendix C), an area of 1 m^2 and a feed flowrate of 5.5 $mol_{H_2O}\,s^{-1}$, where the blue curve corresponds to endothermic operations, the dark red to exothermic operations.

Here, partial pressures are corrected by the component-related compressibility factors, $Z_{\alpha,gas}$, derived in Appendix C.6. Compressibility factors for mixtures, involved in the modeling of CPR1, CPR2 and F2, are denoted by $Z_{mix,gas}$ (Appendix C.7), $Z_{mix,vapor}$ and $Z_{mix,liquid}$ (Appendix C.2) for gas, vapor and liquid mixtures, respectively.

In the following sections, modeling equations shall be denoted with AE/DE.UNIT.NUMBER: algebraic or differential equation, unit operation, number of the equations, respectively.

4.1. SOEC

The SOEC model is zero-dimensional and retrieves the relevant parameters from Udagawa et al. (2007), reported in detail in Appendix C.1. The total power input to the stack ($\dot{W}_{SOEC}$) is expressed as a function of current density, total area and cell voltage:

$$0 = -\dot{W}_{SOEC} + V_{tot,SOEC} A^{(\pi)}_{SOEC} i_{SOEC}, \qquad \text{(AE.SOEC.1)}$$

where the total voltage $V_{tot,SOEC}$ is a summation of ideal (Nernst's) and nonideal contributions (ohmic losses, concentration overpotentials, cathode and anode activation potential), $A^{(\pi)}_{SOEC}$ is the total area of the SOEC, i_{SOEC} is the current density. To solve the system, the activation overpotential at the cathode and anode is expressed as constraints (Udagawa et al., 2007). They are nonlinear functions of exchange current densities $i_{av,cat/an}$ and activation overpotential losses $V_{act,cat/an}$ at cathode and anode, and read as follows:

$$0 = i_{SOEC} + i_{av,cat}\left(\Lambda_1 \exp\left(\Lambda_2 V_{act,cat}\right) - \Lambda_3 \exp\left(\Lambda_4 V_{act,cat}\right)\right), \qquad \text{(AE.SOEC.2)}$$

$$0 = i_{SOEC} + i_{av,an}\left(\exp\left(\Lambda_2 V_{act,an}\right) - \exp\left(\Lambda_4 V_{act,an}\right)\right), \qquad \text{(AE.SOEC.3)}$$

where, for the sake of compactness, the lumping coefficients $\Lambda_{(1-4)}$ are introduced here and expanded in the Appendix C.1. Fig. 5 (A) reports the polarization curves for the single voltage contributions.

Due to the high operating temperature above 1000 K, it is preferable to operate SOEC in adiabatic mode. Consequently, an adiabatic energy balance is added:

$$0 = -\dot{W}_{SOEC} + \dot{H}_{out}(T_{out}) - \dot{H}_{in}(T_{in}), \qquad \text{(AE.SOEC.4)}$$

where inlet and outlet stream enthalpies $\dot{H}_{in,out}$ are functions of the inlet and outlet temperatures, flowrates and compositions, respectively. Fig. 5 (B) shows the outlet temperature, function of the power absorbed. The difference between the inlet and outlet temperatures of SOEC is conservatively constrained to an absolute value of 30 K to avoid extreme temperature gradients along the cathode, which could lead to degradation of the material (Petipas et al., 2013). The SOEC operates at a pressure between 1 and 5 bar and the ideal gas law applies. The input pressure at RWGS is constrained to the operating pressure of SOEC, as given in Table 1 ($p_{in,SOEC} \equiv p_{in,RWGS}$).

4.2. Reactors

Tubular reactors are modeled with steady-state, one-dimensional mass and energy balances, discretized axially by means of the finite-difference upwind scheme with equally spaced nodes. Gas-phase dispersion is neglected. Therefore, it is sufficient to determine the states at the reactor inlet to define the axial profiles. This information comes from the upstream units in the process line. The pressure drop is described by the Ergun equation (Bremer and Sundmacher, 2019). In a recent publication by Seidel et al., a new kinetic model for the methanol synthesis in flexible regimes was proposed and validated, accounting for the relevant fluctuations in CO-to-CO_2 ratios (Seidel et al., 2018). Nonetheless, this study implements the widely accepted model by Graaf et al. (1988), consisting of three kinetic contributions (Graaf et al., 1988) related to Equations (1) - (3) (see Appendix C.5). RWGS implements the kinetics proposed first by Xu and Froment (1989), where three reactions are involved: steam reforming, reverse water-gas shift, and reverse methanation. The chemical relations read, respectively:

$$CH_4 + H_2O \rightleftharpoons CO + 3\,H_2 \qquad \Delta H_R(298\,K) = 205\,kJ\,mol^{-1} \qquad (6)$$

$$CO_2 + H_2 \rightleftharpoons CO + H_2O \qquad \Delta H_R(298\,K) = 42\,kJ\,mol^{-1}, \qquad (7)$$

$$CH_4 + 2\,H_2O \rightleftharpoons CO_2 + 4\,H_2 \qquad \Delta H_R(298\,K) = 163\,kJ\,mol^{-1}. \qquad (8)$$

The model equations in differential form (differential equation, DE) read:

$$0 = -v\frac{d\zeta_\alpha}{dz} + \frac{1-\varepsilon}{\varepsilon}\frac{\rho_{cat}}{C_{gas}}\left(\sigma_\alpha - \zeta_\alpha \sum_{\alpha\in S}\sigma_\alpha\right), \qquad \text{(DE.RWGS.1, DE.METHL.1)}$$

$$0 = -v\varepsilon C_{tot}\tilde{C}_{p,gas}\frac{dT}{dz} + (1-\varepsilon)\,\rho_{cat}\sum_{\alpha\in S} -\tilde{H}_\alpha\sigma_\alpha, \qquad \text{(DE.RWGS.2)}$$

$$0 = -v\varepsilon C_{tot}\tilde{C}_{p,gas}\frac{dT}{dz} - 4\frac{U}{D^{(\pi)}_{T,METHL}}\left(T - T_{cool}\right) + (1-\varepsilon)\,\rho_{cat}\sum_{\alpha\in S} -\tilde{H}_\alpha\sigma_\alpha, \qquad \text{(DE.METHL.2)}$$

$$0 = \frac{dp}{dz} + \frac{(1-\varepsilon)}{\varepsilon^3}\left[150\,v\frac{\varepsilon(1-\varepsilon)}{\left(D^{(\pi)}_{cat,k\in\{RWGS,METHL\}}\right)^2}\mu_{mix} + 1.75\,\rho_{gas}\frac{v^2\varepsilon^2}{D^{(\pi)}_{cat,k\in\{RWGS,METHL\}}}\right], \qquad \text{(DE.RWGS.3, DE.METHL.3)}$$

where ζ_α is the mole fraction of component α, ρ_{cat} is the catalyst density ($1770\,kg\,m^{-3}$ for METHL and $2355\,kg\,m^{-3}$ for RWGS), $\tilde{C}_{p,gas}$ is the molar specific heat at constant pressure in bulk phase (molar average at the discretization node), C_{gas} is the total gas concentration, expressed as Equation (5) for METHL, whereas the ideal gas law is applied to RWGS. Furthermore, σ_α is the source term related to component α, ε is the void fraction ($0.4\,m^3\,m^{-3}$), v is the interstitial velocity stemming from the total mass conservation (derived in Appendix C.9), U is the overall heat transfer coefficient, $\tilde{H}_\alpha$ is the component-related enthalpy of formation at system temperature, μ_{mix} the mixture viscosity obtained from the molar weighted average of component-viscosities at the discretization node. The mass balances DE.RWGS.1 and DE.METHL.1 are derived in Appendix C.10.

The maximum pressure drop is set to 5% of the feed pressure. Mixing node MIX1 imposes that the pressure at the feed to RWGS equals the pressure of SOEC. Furthermore, stream 11 leaving S1 feeds MIX2. An isothermal expansor is implicitly accounted for, as pressure of stream 11 should equal the pressure at stream 10, calculated from the Ergun equation of the RWGS reactor. The METHL reactor is discretized with 300 finite difference nodes, whereas the shorter RWGS adiabatic stage is discretized with 40 nodes (upwind scheme). Therefore, the discretized reactor models contribute to the final nonlinear set of algebraic constraints.

4.3. Mixers, heat exchangers, compressors

In this section, some of the constraints apply with the same formulation to different unit operations in the plant. With an abuse of mathematical notation, such constraints shall be "evaluated at" (vertical bar symbol) the related process elements, whose identifiers are also reported in brackets on the right.

At each stream junction (MIX) represented in Fig. 3, an energy balance determines the outlet temperature:

$$0 = \sum_{i\in I}\sum_{\alpha\in S}\tilde{H}_{i,\alpha}\dot{N}_{i,\alpha} - \sum_{\alpha\in S}\tilde{H}_{o,\alpha}\dot{N}_{o,\alpha}\Big|_{\mathrm{MIX}(1-4)} \qquad \text{(AE.MIX1, AE.MIX2, AE.MIX3, AE.MIX4)}$$

where set I includes all streams entering the node, set S includes all chemical components, and the index o denotes the outflow. Mixers' feed temperatures are not pre-assigned, but result from the solution of the system.

Electric heat exchangers are modeled as functions of two system variables: the outlet temperature and the power input. These units are assumed to be extremely efficient. Therefore, all electric power is converted into thermal energy intended for the process stream. The governing equation reads:

$$0 = -\dot{W}_{HE} + \sum_{\alpha\in S}\left(\int_{T_{in}}^{T_{out}}\tilde{C}_{p,\alpha}\dot{N}_{in,\alpha}\,dT\right) \qquad \text{(AE.HE1, AE.HE2, AE.HE3)}$$

with the addition of the latent heat of vaporization of water at 298 K for the case of HE1: $\Delta H_{ev}(298\,K)$.

Compressors are modeled as a sequence of isentropic compression stages: adiabatic and reversible. Two governing equations express the relation among three system variables: power input, discharge temperatures and pressure. The first defines the power required by the individual stage of compressor CPR1 and CPR2 (Lüdtke, 2004; Nederstigt and Pecnik, 2023):

$$0 = -\dot{W}_{CPR(stage)} + \left(\sum_{\alpha\in S}\dot{N}_{in,\alpha}\right)R_{gas}T_{in}Z_{mix,gas}\frac{\kappa_{av}}{\kappa_{av}-1}\left[\left(\frac{p_{out}}{p_{in}}\right)^{\left(\frac{\kappa_{av}-1}{\kappa_{av}}\right)}-1\right]\frac{1}{\eta_{CPR}} \qquad \text{(AE.CPR1.1, AE.CPR2.1)}$$

where the cubic equation of state is solved analytically for the compressibility factor of the mixture, $Z_{mix,gas}$ (see Appendix C.6), and the ratio of the temperature-dependent specific heat capacities at constant pressure and at constant volume determines κ. The average value of κ between inlet and outlet stream is denoted as κ_{av}. The isentropic efficiency η_{CPR} is usually determined from the manufacturer's product information. In absence of this information, the efficiency is here assumed to be one. The second relation reads:

$$0 = T_{out} - T_{in}\left(\frac{p_{out}}{p_{in}}\right)^{\frac{\kappa_{av}-1}{\kappa_{av}}} \qquad \text{(AE.CPR1.2 AE.CPR2.2)}$$

and binds the temperature and pressure ratios of inlet and outlet flows. Equations (AE.CPR1.1, AE.CPR2.1) and (AE.MIX1, AE.MIX2, AE.MIX3, AE.MIX4) are repeated for the number of compression stages for CPR1 and CPR2.

The intermediate coolers are not modeled directly, since it is assumed that enough cold utility is available to bring the temperature of the feed to the next compression stage to 298 K. This decision does not apply to the last compression stage, whose isentropic outlet temperature is directly exploited by the next process item – heat exchanger HE3.

4.4. Flash separators

Flash F1 is run at a pressure range comparable to that of RWGS and SOEC. The preceding cooling step CL3 allows the temperature to drop to ambient temperature before the separator F1.

The Rachford-Rice equation in ξ, namely, the ratio between vapor and feed flowrates, is implemented to allow partial separation of water from all other components:

$$0 = \sum_{c\in C}\frac{\zeta_{feed,c}\left(K_c-1\right)}{\alpha K_c+(1-\xi)} + \frac{\sum_{i\in I}z_i}{\xi} \qquad \text{(AE.F1.1, AE.F2.1)}$$

where set I includes the incondensable components, whereas set C includes exclusively water (condensable component). Due to the low pressure range, Raoult's law applies for the determination of the distribution coefficient K_c.

Flash F2 comes after throttling. The attained pressure level is higher than for F1. Consequently and also due to the low temperature, mixing rules are applied to RKS. In flash F2, set C includes water and methanol. For this flash separator, the equilibrium constant K_c results from a direct approach:

$$K_c = \frac{\Phi_{c,liquid}}{\Phi_{c,vapor}}, \qquad (9)$$

where the fugacity coefficient for component c in liquid and vapor phase is determined as reported in Appendix C.2, Equation (C.5). In addition to the Rachford Rice equation (AE.F2.1), this model incorporates two cubic equations in the compressibility factor $Z_{mix,vap/liq}$, one initialized with a higher value (largest root for vapor phase, of value one), the other with a low value (smaller root for liquid phase, a positive infinitesimal). They read:

$$0 = Z_{mix,vap}^3 + \alpha_{mix,vap}Z_{mix,vap}^2 + \beta_{mix,vap}Z_{mix,vap} + \gamma_{mix,vap}, \qquad \text{(AE.F2.2)}$$

$$0 = Z_{\mathrm{mix,liq}}^3 + \alpha_{\mathrm{mix,liq}} Z_{\mathrm{mix,liq}}^2 + \beta_{\mathrm{mix,liq}} Z_{\mathrm{mix,liq}} + \gamma_{\mathrm{mix,liq}}. \quad \text{(AE.F2.3)}$$

Coefficients for the cubic equations are based on mixing rules and expanded in Appendix C.

5. Optimization objectives, scenarios and solver

5.1. Objective functions

In this study, design and operation of a flexible Power-to-Methanol plant are compared with the results of a single-period optimization at the yearly-averaged nominal load, achieved by means of buffering strategies. This comparison is based on profitability, which is an important performance indicator when investigating industrial applications. Heat integration can help redefine the power distribution between plant units, thus influencing the resulting values of the optimization variables. In addition, the plant can be designed at the maximum Power-to-Methanol efficiency, achievable regardless of the profit and independent of fixed costs. All this considered, three optimization objectives are defined:

1. maximum profit for flexible plant operations (multi-period);
2. maximum profit for plant operations in steady-state with large electricity or hydrogen buffers (single-period);
3. maximum Power-to-Methanol efficiency for steady state operations, defined as the ratio between lower-heating value of the methanol outlet flowrate and the power input to the plant (single-period), not accounting for the distillation duty.

Objective 1. relating to the multi-period case reads:

$$\max_{\boldsymbol{x}^{(\pi)},\bar{\tilde{\boldsymbol{x}}}} \sum_{j\in\{1,\mathrm{NP}\}} \omega_j \left(\dot{C}_{22,\mathrm{CH_3OH},\Pi_j} - \sum_{i\in\mathrm{UNITS}} \dot{C}_i^{(\pi)} \right), \quad \text{(OBJ.PROFIT.MP)}$$

where $j \in \{1, \mathrm{NP}\}$ and Π_j identify the period, $i \in$ UNITS the installation cost of reactor tubes and catalyst for METHL and RWGS, and the installation cost of SOEC based on the total power consumed. Vector $\boldsymbol{x}^{(\pi)}$ and $\bar{\tilde{\boldsymbol{x}}}$ include all design and operation variables for all periods, respectively, where the latter is intended as a collection of vectors for different periods and is indicated by a bar hat above the symbol. This vector reads:

$$\bar{\tilde{\boldsymbol{x}}} = \left[\tilde{\boldsymbol{x}}_1, \tilde{\boldsymbol{x}}_2, .., \tilde{\boldsymbol{x}}_{\mathrm{NP}}\right], \quad (10)$$

where vector $\tilde{\boldsymbol{x}}_j$ is the set of operation variables and states for the generic j-th period. In addition, a tilde-hat distinguishes the full set of operation variables from the set of design variables. Heat exchangers, coolers, flash drums and compressors are assumed to be flexible so that they can always meet the requirement of each possible operating framework: their size remains unvaried throughout the different flexibility cases. Therefore, the selection of these units is independent on the optimization objectives and their costs do not contribute to OBJ.PROFIT.MP, as their optimization does not contribute to the comparative analysis of flexibility cases. For the same reason, the levelized cost of the wind farm does not contribute to the optimization scenarios. As a consequence, while it is true that the profit is optimized, the objective functions discussed in this section are pseudo-profits, i.e., the profit scaled up due to the fact that such process items are not included in the optimization. For the modeling of capital costs of RWGS and METHL (reactor vessels and tubes), Guthrie and Timmerhaus cost functions are adopted, actualized to 2022 (CEPCI index) and annualized (fixed cost divided by the expected lifetime). Cost formula and prices follow in Appendix D.

For the single-period optimization but the same objective function, Objective 2. reads:

$$\max_{\boldsymbol{x}^{(\pi)},\tilde{\boldsymbol{x}}} \left(\dot{C}_{22,\mathrm{CH_3OH}} - \sum_{i\in\mathrm{UNITS}} \dot{C}_i^{(\pi)} \right), \quad \text{(OBJ.PROFIT.SP)}$$

where now also operation variables are reported in vector form and the bar hat no longer appears. Therefore, Objective 3. is equivalent to maximizing the methanol flowrate in stream 22, outlet of the entire upstream-conversion section of the plant:

$$\max_{\boldsymbol{x}^{(\pi)},\tilde{\boldsymbol{x}}} \left(\eta_{\mathrm{PtCH_3OH}} \right) = \max_{\boldsymbol{x}^{(\pi)},\tilde{\boldsymbol{x}}} \left(\frac{\dot{N}_{22,\mathrm{CH_3OH}} \mathrm{LHV}_{\mathrm{CH_3OH}}}{\dot{W}_{\mathrm{tot}}} \right) = \max_{\boldsymbol{x}^{(\pi)},\tilde{\boldsymbol{x}}} \left(\dot{N}_{22,\mathrm{CH_3OH}} \right). \quad \text{(OBJ.EFF.SP)}$$

Objective functions (OBJ.PROFIT.MP), (OBJ.PROFIT.SP) and (OBJ.EFF.SP) are implemented to explore promising plant configurations and operational strategies in a rational sequence of case-studies.

5.2. Case-studies

At first, the design and operations for the maximum profit shall be identified in the context of buffering scenario F, in which maximum plant flexibility is involved – case-study: CASE.FLEX. Multi-period optimization is here applied. Thereafter, single-period optimization is applied to evaluate the buffering strategy B.I (electricity storage) and B.II (hydrogen storage) in case-study CASE.BUFF. Results of CASE.BUFF and CASE.FLEX are then compared. In CASE.BUFF, the plant is designed for a power rating of 23.5 MW, obtained by integration of the product between the probability density function and the power curve in Fig. 4. In discretized form, it is the product between the average power delivered by the wind farm at consecutive discretization points along the abscissa (wind velocity), and the integral probability of occurrence for that segment, over the entire domain of wind velocities (from $0\,\mathrm{m\,s^{-1}}$ to $25\,\mathrm{m\,s^{-1}}$). For the adopted set of 50 equally-spaced discretization nodes, it reduces to:

$$\dot{W}_{\mathrm{tot(B.I,B.II)}} = \sum_{i\in\{2,50\}} \frac{\left(\dot{W}_{\mathrm{tot},i} + \dot{W}_{\mathrm{tot},i-1}\right)\left(\omega_i + \omega_{i-1}\right)\left(v_{\mathrm{wind},i} - v_{\mathrm{wind},i-1}\right)}{4}, \quad (11)$$

where ω_i is the value at discretization point i of the probability density function (Fig. 4), $\dot{W}_{\mathrm{tot},i}$ and $v_{\mathrm{wind},i}$ represent, respectively, the power generated by the wind park and the wind velocity. In Fig. 4, this annual averaged power supply is identified by the dashed-dotted orange horizontal line.

The power integrated at period Π_1 for flexible operations (B.I) is obtained by subtracting the weighted integral of the renewable power curve within the period (as shown in Equation (11), between $0\,\mathrm{m\,s^{-1}}$ and $6.45\,\mathrm{m\,s^{-1}}$) from the power actually supplied, stable at 25% of the nominal power supplied by the wind park (discussed at the beginning of Section 3).

For this analysis, installation costs of storage devices disregard the actual yearly wind velocity series: it is assumed that the maximum surplus of renewable energy can be determined by the longest time spent by the wind park at its nominal (i.e., maximum) power output at 50.5 MW, for wind velocities comprised between $12\,\mathrm{m\,s^{-1}}$ and $25\,\mathrm{m\,s^{-1}}$. Afterwards, in a new scenario CASE.EFF, the Power-to-Methanol efficiency maximized for the single period at mean wind velocity (OBJ.EFF.SP) is compared with the corresponding value obtained in CASE.FLEX. This allows to indicate how efficiency is lost in the multi-period maximization of the profit (CASE.FLEX). Finally, the results of CASE.FLEX are reconsidered and compared within the same framework, that is, multi-period maximization of the profit, with the implementation of heat integration – case-study CASE.FLEX.HI. Temperature levels are not considered in this theoretical benchmark, which provides an upper bound to the benefits of heat integration. Consequently it is assumed that, the whole amount of thermal power is recoverable from cold utilities within the plant and is utilized for the vaporization of water and preheating at the inlet of SOEC. Table 2 summarizes relevant aspects related to the four optimization cases here presented.

Table 2
Summary of the case-studies.

case study	objective	method	heat integration	buffering scheme
CASE.FLEX	(OBJ.PROFIT.MP)	multi-period	no	F
CASE.BUFF	(OBJ.PROFIT.SP)	single-period	no	B.I,B.II
CASE.EFF	(OBJ.EFF.SP)	single-period	no	B.I,B.II
CASE.FLEX.HI	(OBJ.PROFIT.MP)	multi-period	yes	F

Table 3
Overview of the problem size: number of variables, constraints and resulting degrees of freedom.

	variables	equality constraints	degrees of freedom	number of variables: design, operation	number of periods
NLP.FLEX	13785	13675	110	10, 100	5
NLP.BUFF	2765	2735	30	10, 20	1
NLP.EFF	2765	2735	30	10, 20	1
NLP.FLEX.HI	13785	13675	110	10, 100	5

5.3. Final NLPs and problem size

Modeling constraints, objective functions and scenario settings being introduced (Section 4 and 5.1, respectively), this section reports the final formulation of the NLP problems in differential form. Nonlinear problems are denoted by NLP.{FLEX,BUFF,EFF,FLEX.HI}, which translate case-studies CASE.{FLEX,BUFF,EFF,FLEX.HI} introduced in Section 5.2 into mathematical notation. The NLP associated with the first multi-period optimization scenario (CASE.FLEX) reads:

$$\max_{\boldsymbol{x}^{(\pi)},\overline{\tilde{\boldsymbol{x}}}} \quad \sum_{j\in\{1,\mathrm{NP}\}} \omega_j \left(\dot{C}_2 2, \mathrm{CH_3OH}, \Pi_j - \sum_i \in \mathrm{UNITS}\dot{C}^{(\pi)}{}_i \right)$$

s.t. **AE**.Wtot, (NLP.FLEX)

AE.SOEC.(1, 2, 3, 4),

DE.RWGS.(1, 2, 3), **DE**.METHL.(1, 2, 3),

AE.MIX1, **AE**.MIX2, **AE**.MIX3, **AE**.MIX4,

AE.HE1, **AE**.HE2, **AE**.HE3,

AE.CPR1.(1, 2), **AE**.CPR2.(1, 2),

AE.F1.1, **AE**.F2.(1, 2, 3)

$|\boldsymbol{T}_{\mathrm{out,SOEC}} - \boldsymbol{T}_{\mathrm{in,SOEC}}| \le 30\,\mathrm{K}$,

$\boldsymbol{p}_{\mathrm{in,RWGS}} = \boldsymbol{p}_{\mathrm{out,SOEC}}$,

$p_{\mathrm{in,(RWGS,METHL)}} - \boldsymbol{p}_{\mathrm{out,(RWGS,METHL)}} / p_{\mathrm{in,(RWGS,METHL)}} \le 0.05$,

$0.05\,\mathrm{m\,s^{-1}} \le \boldsymbol{v}_{\mathrm{(RWGS,METHL)}} \le 3\,\mathrm{m\,s^{-1}}$,

$\boldsymbol{p}_{\mathrm{out,CPR1}} = \boldsymbol{p}_{\mathrm{out,CPR2}}$,

$\boldsymbol{T}_{\mathrm{METHL}} \le 600\,\mathrm{K}$,

$\boldsymbol{T}_{\mathrm{out,TR}} \ge 230\,\mathrm{K}$,

$\zeta_{\mathrm{CH_4}}, \mathrm{METHL} \le 0.01$.

$\{\boldsymbol{x}^{(\pi)}, \overline{\tilde{\boldsymbol{x}}}\} \le \{\mathbf{UBX}^{(\pi)}, \widetilde{\overline{\mathbf{UBX}}}\}$,

$\{\boldsymbol{x}^{(\pi)}, \overline{\tilde{\boldsymbol{x}}}\} \ge \{\mathbf{LBX}^{(\pi)}, \widetilde{\overline{\mathbf{LBX}}}\}$,

where bold entries constitute sets of constraints (**AE**, **DE**), vectors of system variables, the latter being denoted by a bar hat if they are not shared across periods, as discussed in Section 5.1. Set $\mathbf{AE}.W_{\mathrm{tot}}$ collects replicas of Equation (AE.Wtot) across periods (AE.Wtot), where the total power is defined as in Equation (4).

The second and third optimization cases, CASE.BUFF and CASE.EFF, refer to the same set of constraints in single-period, with different objective functions, respectively, (OBJ.PROFIT.SP) and (OBJ.EFF.SP). In single-period optimization, constraints and operation variables are no longer replicated across periods. The NLPs read:

$$\max_{\boldsymbol{x}^{(\pi)},\tilde{\boldsymbol{x}}} \quad \left(\dot{C}_2 2, \mathrm{CH_3OH} - \sum_i \in \mathrm{UNITS}\dot{C}^{(\pi)}{}_i \right) \text{ and } \left(\dot{N}_2 2, \mathrm{CH_3OH} \right)$$

s.t. AE.Wtot, (NLP.BUFF and NLP.EFF)

AE.SOEC.(1, 2, 3, 4),

DE.RWGS.(1, 2, 3), DE.METHL.(1, 2, 3),

AE.MIX1, AE.MIX2, AE.MIX3, AE.MIX4,

AE.HE1, AE.HE2, AE.HE3,

AE.CPR1.(1, 2), AE.CPR2.(1, 2),

AE.F1.1, AE.F2.(1, 2, 3)

$|T_{\mathrm{out,SOEC}} - T_{\mathrm{in,SOEC}}| \le 30\,\mathrm{K}$,

$p_{\mathrm{in,RWGS}} = p_{\mathrm{out,SOEC}}$,

$p_{\mathrm{in,(RWGS,METHL)}} - p_{\mathrm{out,(RWGS,METHL)}} / p_{\mathrm{in,(RWGS,METHL)}} \le 0.05$,

$0.05\,\mathrm{m\,s^{-1}} \le v_{\mathrm{(RWGS,METHL)}} \le 3\,\mathrm{m\,s^{-1}}$,

$p_{\mathrm{out,CPR1}} = p_{\mathrm{out,CPR2}}$,

$T_{\mathrm{METHL}} \le 600\,\mathrm{K}$,

$T_{\mathrm{out,TR}} \ge 230\,\mathrm{K}$,

$\zeta_{\mathrm{CH_4}}, \mathrm{METHL} \le 0.01$.

$\{\boldsymbol{x}^{(\pi)}, \tilde{\boldsymbol{x}}\} \le \{\mathbf{UBX}^{(\pi)}, \widetilde{\mathbf{UBX}}\}$,

$\{\boldsymbol{x}^{(\pi)}, \tilde{\boldsymbol{x}}\} \ge \{\mathbf{LBX}^{(\pi)}, \widetilde{\mathbf{LBX}}\}$.

The formulation of the last multi-period problem with heat integration, NLP.FLEX.HI, is equivalent to the formulation of Problem NLP.FLEX (multi-period, without heat integration). In addition, the power recovered from cold utilities is subtracted from the heating duty for HE1, the circulating heat exchanger SOEC inlet. Therefore, the constraint AE.HE1 for the heat exchanger at the SOEC inlet, becomes:

$$0 = \dot{W}_{\mathrm{HE1}} - \left[\left(\int_{298\,\mathrm{K}}^{T_{\mathrm{SOEC}}} \tilde{C}_{\mathrm{p,H_2O}} \dot{N}_{\mathrm{in,H_2O}} dT \right) + \Delta H_{\mathrm{ev}}(298\,\mathrm{K}) - \left(\dot{Q}_{\mathrm{CL1}} + \dot{Q}_{\mathrm{CL2}} + \dot{Q}_{\mathrm{CL3}} + \dot{Q}_{\mathrm{CL4}} \right) \right], \tag{12}$$

which includes the sum of all recoverable thermal power output from the plant cooling devices, CL(1-4). The size of these NLPs is reported in Table 3.

5.4. Solver

The system is modeled in MATLAB2018b, which invokes IPOPT (Wächter and Biegler, 2006) via CasADi (Andersson, 2013; Andersson et al., 2019) v3.5.5 for the solution of large NLPs, running on the linear solver MA97 (HSL, 2007). Computations are performed on a Linux machine, processor Intel^{R} Core^{TM} i7-6700 CPU @ 3.4 GHz, 4 cores, each provided with 8 GB RAM. The numerical sensitivity of the results is tested by changing solver tolerances and making use of multi-start procedures.

6. Optimization results

This section reports and discusses optimization results obtained from the implementation of the four NLPs. A quantitative and comprehensive overview of the results of the different scenarios is reported in Table 4 and Table 5, which illustrate the optimal design and operating variables, costs of the optimized units, and revenues.

From a topological perspective common to all scenarios and represented in Fig. 6, the RWGS reactor is excluded from all optimization solutions. From a numerical perspective though, this reactor is still present with a negligible volume, and a very small purge stream 24 is fed with a negligible flowrate as, in this modeling approach, no integer formulation allowed for zero-flow streams: removing stream 24 completely from the flowsheet would not allow for convergence of the NLP optimizations. In practice, splitter S1 deviates the whole SOEC outlet away from RWGS, and the feed stream of carbon dioxide bypasses this reactor. Split factor S2 enforces a closed recycle loop after the methanol reactor. A dedicated RWGS reactor would introduce inert methane in the METHL loop, as prescribed by the kinetic model by Xu et al. in Appendix C.4. This would imply larger unit operations and purge stream 24 after splitter S2 to be active. Therefore, not only methane, but also part of the valuable non-condensable reactants would be purged. In particular, an additional power requirement at the SOEC would be required to compensate for the loss in hydrogen. Furthermore is to be observed that, although the RWGS reactor presents a negligible volume, carbon monoxide recirculates within the methanol loop. The presence of carbon monoxide in the METHL reactor is enforced due to kinetic reasons, as it enhances the mass action related to its hydrogenation towards methanol (Appendix C.5). This path does not produce water which, in turn, hinders the equilibrium of the parallel reaction to methanol via carbon dioxide hydrogenation. The latter reaction path contributes to the overall kinetics due to its lower exothermicity, determining lower temperatures, thus favoring thermodynamics. At the same time, carbon monoxide is regenerated as a result of the reverse water-gas shift contribution to the kinetic model of the methanol synthesis.

Fig. 7 (**A**), reporting results at the highest load-period, shows that the net generation of carbon monoxide along the axis of the METHL reactor is negative until the temperature hot spot is attained (see Fig. 8 in the following section). In this region, the conversion of carbon monoxide to methanol is faster than its generation from the reverse water-gas shift contribution, as the exothermicity of the former reaction drags the latter (endothermic) reaction. After the hot spot is attained, the trend reverses. The net generation rate shows a positive maximum as reverse water-gas shift dominates. Afterwards, the system tends to stabilize towards the thermodynamic equilibrium dictated by the coolant temperature. As expected, the same trend is reflected by the molar flowrate of carbon monoxide in Fig. 7 (**B**). Essentially, its molar flowrate does not vary between reactor inlet and outlet. Fig. 7 (**C**) reports the molar flowrate of carbon dioxide along the reactor axis, which is substantially converted until the proximity to the outlet, also due to its contribution to reverse water-gas shift. A different reactivity in the METHL reactor, more selective toward methanol and with a weaker tendency towards reverse water-gas shift, would result in the need to compensate for the loss of carbon monoxide by adding the RWGS reactor upstream.

6.1. Results for CASE.FLEX: maximum flexibility without heat integration

Fig. 8 shows relevant trends along the axial coordinate of METHL for the different periods. Temperature profiles (tube side) and cooling temperatures (shell side) are directly proportional to the feed flowrates and to the velocity profiles, the latter determining proportional pressure drops. The feed pressure ranges between 51.1 bar and 56.8 bar. The cooling temperature ranges between 508 K and 536 K. The composition profiles show no qualitative differences for the different periods, as their trends are essentially preserved. The methanol yield per pass based on carbon dioxide, thus defined as the ratio between moles of carbon dioxide consumed and moles of methanol generated in the reactor, is one, whereas the conversion of carbon dioxide and hydrogen per pass range within 20-25% and 17-21%, respectively. The outlet mole fraction of methanol ranges between 4.4% and 6% and is inversely proportional to the load, which is justified by the lower residence times at higher feed flowrates. The resulting design for METHL consists of a bundle of 508 tubes of length 9.53 m and diameter 5.2 cm, with a total volume of 10.5 m^3. The diameter of the catalyst particle is 1/10 of the tube diameter, due to a dedicated constraint. The molar ratio between liquid water and methanol in stream 22 prior to distillation is essentially unvaried (1.02), which validates the assumption reported in Section 2.2 on time-independent composition of the feed to the distillation unit. Similarly, in CASE.FLEX.HI this ratio stands around a value of 1.03.

The SOEC is operated exclusively in the endothermic reaction regime, at the limit of the permitted temperature drop between inlet and outlet section, 30 K. This value exceeds the temperature difference range shown in Fig. 5 (**B**), as it results from a different area of SOEC and feed flowrate from the simulation results of the single unit operation. Fig. 9 shows the direct proportionality between the resulting current density, voltage, feed temperature and operating pressure with the corresponding period. In Table 4, the supply temperature to the SOEC is equivalently reported as the outlet temperature from the first heat exchanger ($T_{out,HE1}$). The SOEC area is 2155 m^2.

The flash separator F2 separates most of the condensable water and methanol due to the very low temperatures achievable with throttling, due to the low pressure attained after isenthalpic expansion of the off-gases from the METHL reactor. The pressure drop at the throttling valve is comprised between 54% and 57% of its feed pressure. Fig. 10 is a logarithmic representation of the partition of the total power in the plant among the unit operations. Clearly, the largest duty is reserved for SOEC operations. A large amount of power is required for steam generation and preheating in the HE1 heat exchanger for SOEC supply. This bottleneck can be reduced if heat-integration is enforced with the cold process streams, as proposed for CASE.FLEX.HI.

The achievable product flowrate from the plant ranges between 33 and 127 $ton\,day^{-1}$, where 69 $ton\,day^{-1}$ is the annual weighted average productivity. Considering a prevailing selling price of methanol of 580 €/ton^{-1}, as in the first quarter of 2022 in Germany (Methanol Price Trend and Forecast., 2022), the revenue reads as in Fig. 11 (A), where the dashed horizontal line refers to average revenue (left y-axis) and average productivity (right y-axis).

Together with the revenues, results identify annualized and actualized installation costs for the optimized unit operations, represented by the green bars in Fig. 11 (B) and reported in Table 5. The cost of RWGS is negligible, whereas SOEC accounts for the largest contribution. This also derives from the higher turnover of unit replacement, 2 years, reported in Anghilante et al. (2018).

Below the selected power level associated with Π_1 and equivalent to 25% of the maximum power supply, NLP.FLEX failed to identify a feasible solution. This indicates that, for loads lower than $\dot{W}_{\Pi_1}$, the con-

Table 4

Optimization results for the case-studies listed in Table 2. Reactor volumes, reported in brackets, are calculated from the results, i.e., they do not constitute decision variables. The table continues under the thicker dividing-line, where $\dot{N}_{tot,(1,5,6)}$ represent, respectively, the feed stream of water, carbon dioxide to RWGS, carbon dioxide to the methanol loop.

case-study	Π	P_{CH_3OH} $ton_{CH_3OH}\,day^{-1}$	Design Variables$^{(\pi)}$							
			$A^{(\pi)}_{SOEC}$ m^2	$L^{(\pi)}_{T,RWGS}$ m	$D^{(\pi)}_{T,RWGS}$ m	$(V^{(\pi)}_{RWGS})$ m^3	$N^{(\pi)}_{T,METHL}$ –	$L^{(\pi)}_{T,METHL}$ m	$D^{(\pi)}_{T,METHL}$ m	$(V^{(\pi)}_{METHL})$ m^3
CASE.FLEX	1	33.142	2155	1.024		(8.1×10^{-3})	508	9.537	5.2×10^{-2}	(10.471)
	2	47.700								
	3	85.396			1.00×10^{-1}					
	4	119.483								
	5	126.802								
	annual	69.412								
CASE.BUFF (23.5 MW)	1	60.404	3904	1.254	1.01×10^{-1}	(1×10^{-2})	321	13.4	4.9×10^{-2}	(8.22)
CASE.EFF (23.5 MW)	1	63.457	4129	1.7	1.00×10^{-1}	(1.32×10^{-2})	3039	15	6.8×10^{-2}	(165.9)
CASE.FLEX.HI	1	36.875	2375	1.75	1.00×10^{-1}	(1.38×10^{-2})	64	15	1.49×10^{-1}	(16.9)
	2	52.387								
	3	94.977								
	4	132.461								
	5	140.932								
	annual	77.042								

	Π	Operation Variables								
		$\dot{N}_{tot,(1,5,6)}$ $mol\,s^{-1}$	$T_{out,HE_{1,2,3}}$ K	$\boldsymbol{p}_{out,(stage),CPR1}$ bar	$\boldsymbol{p}_{out,(stage),CPR2}$ bar	$p_{in_{SOEC,RWGS}}$ bar	$p_{in,METHL}$ bar	$T_{cool,METHL}$ K	S1 –	S2 –
CASE.FLEX	1	36.2, 0.014, 12.0	1000, 1001, 478	4.4 (1-4) ,51.1 (5)	23.0 (1-3), 23.1 (4), 51.1 (5)	4.39	51.1	508	3.9×10^{-4}	1.3×10^{-4}
	2	52.2, 0.027, 17.2	1022, 994, 478	4.4 (1-2), 4.5 (3), 4.6 (4) ,51.1 (5)	23.0 (1-2), 23.1 (3-4), 52.4 (5)	4.30	52.4	519	6.0×10^{-4}	2.7×10^{-4}
	3	93.3, 0.026, 30.9	1061, 995, 478	4.6 (1-2), 4.7 (3-4), 54.2 (5)	23.0 (1-4), 54.2 (5)	4.58	54.2	527	3.2×10^{-4}	4.8×10^{-5}
	4	130.5, 0.034, 43.2	1085, 992, 478	4.7 (1), 4.8 (2-3), 4.9 (4), 56.5 (5)	23 (1-4), 56.5 (5)	4.65	56.5	535	3.0×10^{-4}	3.0×10^{-5}
	5	138.5, 0.033, 45.8	1089, 993, 478	4.8 (1-2), 4.9 (3-4), 56.8 (5)	23.0 (1-4), 56.8 (5)	4.75	56.8	536	2.8×10^{-4}	7.2×10^{-6}
CASE.BUFF (23.5 MW)	1	66.1, 0.034, 21.8	1000, 992, 477	4.4 (1), 4.6 (2), 4.7 (3), 4.9 (4), 55.8 (5)	23.0 (1), 23.1 (2-4), 55.8 (5)	4.31	55.8	529	6.1×10^{-4}	2.8×10^{-4}
CASE.EFF (23.5 MW)	1	69.3, 0.010, 22.9	1000, 1009, 477	5.0 (1-4), 48.0 (5)	23.0 (1-4), 48.0 (5)	4.95	48.0	480	6.8×10^{-5}	1.6×10^{-7}
CASE.FLEX.HI	1	40.5, 0.044, 13.3	1000, 976, 519	10.1, 17.5, 25.7, 35.0, 49.9	27.1, 31.6, 36.3, 41.4, 49.9	3.09	49.9	492	1.3×10^{-3}	8.9×10^{-4}
	2	57.7, 0.063, 19.0	1020, 858, 519	9.5, 17.2, 25.9, 35.9, 51.4	27.3, 31.9, 36.8, 42.2, 51.4	3.04	51.4	506	1.4×10^{-3}	1.1×10^{-3}
	3	104.3, 0.064, 34.4	1061, 868, 519	10.5, 18.4, 27.1, 37.0, 52.2	27.4, 32.0, 37.1, 42.5, 52.2	3.25	52.2	504	8.0×10^{-4}	5.0×10^{-4}
	4	145.4, 0.070, 47.9	1084, 809, 519	10.8, 18.9, 28.0, 38.4, 53.9	27.6, 32.4, 37.7, 43.4, 53.9	3.32	53.9	511	6.4×10^{-4}	3.9×10^{-4}
	5	154.5, 0.067, 51.0	1089, 864, 519	11.8, 19.8, 28.7, 38.9, 54.0	27.6, 32.4, 37.7, 43.4, 54.0	3.45	54.0	510	5.6×10^{-4}	2.7×10^{-4}

Table 5
Optimization results. $\dot{C}_{22,CH_3OH}$ annual revenue from selling methanol at 580 €/ton^{-1}, prevailing price for the first quarter of 2022 in Germany (Methanol Price Trend and Forecast., 2022). Cost $\dot{C}^{\Delta}_{Plant}$ incorporates the process units subject to optimization (SOEC, RWGS, METHL). All costs are annualized, i.e., the absolute cost divided the expected number of years of operations.

case-study	Π	$\dot{C}_{22,CH_3OH}$	η_{PtCH_3OH}	$\dot{C}^{\Delta}_{Plant}$	$\dot{C}^{(\pi)}_{SOEC}$ 2 years	$\dot{C}^{(\pi)}_{RWGS}$		$\dot{C}^{(\pi)}_{METHL}$		$\dot{C}_{buffering\ device}$ 12 h peak(1) 24 h peak(2)	
						tube 10 years	catalyst 2 years	tube bundle 10 years	catalyst 2 years	Li-ion(a) 10 years	H_2 tank(b) 10 years
CASE.FLEX	1	7 016 230	60.5%	1 696 183	1 164 294	177	117	134 443	397 152	-	-
	2	10 098 010	59.6%								
	3	18 078 350	58.6%								
	4	25 294 736	57.9%								
	5	26 844 032	57.8%								
	annual	14 694 648									
CASE.BUFF (23.5 MW)	1	12 787 612	59.2%	5 882 874(a1) 2 073 244(b1) 10 321 674(a2) 2 526 118(b2)	1 012 730	210	147	119 051	311 936	4 438 800 8 877 600	629 170 1 082 044
CASE.EFF (23.5 MW)	1	13 433 982	62.2%	12 532 238(a1) 8 722 608(b1) 16 971 038(a2) 9 175 482(b2)	1 062 601	262	192	736 959	6 293 424	4 438 800 8 877 600	629 170 1 082 044
CASE.FLEX.HI	1	7 806 601	67.3%	2 028 551	1 294 898	272	202	91 435	641 744	-	-
	2	11 090 451	65.5%								
	3	20 106 823	65.3%								
	4	28 042 199	64.2%								
	5	29 835 414	64.3%								
	annual	16 309 948									

straints cannot be satisfied due to infeasible plant operations. The red bars shown in Fig. 11 (B) represent the annual cost of external power, integrated to sustain plant operations for period Π_1 under three distinct pricing scenarios. Electricity prices are arbitrary but representative values for the different cases reported and commented in Section 6.2.1, where the comparative analysis of the current case-study (integration of external power to the plant) and the results of CASE.BUFF (implementation of electricity or hydrogen buffering, respectively, B.I and B.II) is proposed.

6.2. Results for CASE.BUFF: steady-state operations without heat integration

Electricity (B.I) and hydrogen buffers (B.II) must be sized to ensure steady-state plant operations at the nominal, yearly-averaged power supply of 23.5 MW, despite the fluctuations of the renewable resource. The actual time series of a renewable power provision would allow for the rigorous identification of the maximum amount of electricity to be stored and, consequently, the exact size of buffers. Nevertheless, this level of detail in the sizing procedure is not accounted for, as the methodology and the quality of the comparison between buffering strategies remain essentially unchanged. Instead, the size of buffering devices is determined by the maximum time spent by the wind park at its maximum power output within a single loading cycle, which is equal to 50.5 MW, i.e., 27 MW above the design load for the chemical plant. This information allows to estimate the maximum energy stored as $E_{stored} = 27\,\mathrm{MW} t_{buff}$, where t_{buff} spans between 0 hr and 24 hr. Due to a further simplification related to hydrogen buffering analysis (strategy B.II), multi-period design optimization of the sole SOEC unit is neglected, although the electrolyzer should in this case follow the fluctuating trend of renewable power supply. For simplicity, the unit is set to a single load throughout the year.
The cost of lithium batteries is 137 €/kWh^{-1}, as reported in Zakeri and Syri (2015). Clearly, lithium batteries do not constitute the only technical solution, and they were selected as a reference case due to their widespread availability. In contrast, determining the amount of excess energy is not sufficient to estimate the fixed costs related to the storage of hydrogen. In fact, the surplus is to be shared among three power sinks: the preconditioning of steam at the SOEC (vaporization and preheating), the SOEC electrolysis itself and the compression work for the storage of hydrogen at 300 bar. The sum of precondition and electrolyzer power demand at SOEC is divided by the molar flowrate of hydrogen resulting from the unit to get λ_{SOEC}, which reads:

$$\lambda_{SOEC} = \frac{\dot{W}_{HE1} + \dot{W}_{SOEC}}{\dot{N}_{prod,H_2}} = 0.3156\,\mathrm{MJ\,mol}^{-1}_{H_2}, \tag{13}$$

essentially constant for different scenarios, as verified from the analysis of results of NLP.FLEX at different loads. The specific molar compression work to store hydrogen at 300 bar is denoted by $\psi_{compression,300\,bar} = 0.019\,42\,\mathrm{MJ\,mol}^{-1}_{H_2}$. Therefore, the molar flowrate of buffered hydrogen reads:

$$\dot{N}_{buff,H_2} = \frac{50.5\,\mathrm{MW}_{peak} - 23.5\,\mathrm{MW}_{nominal,plant}}{\left(\lambda_{SOEC} + \psi_{compression,300\,bar}\right)}. \tag{14}$$

Ultimately, Equation (14) defines the amount of hydrogen produced with the maximum excess power, and accounts for the generation and preheating of steam, the SOEC demand and the hydrogen compression duty. Thus, it is possible to calculate the moles of hydrogen stored as a function of the maximum loading time, t_{buff}:

$$N_{buff,H_2}(t_{buff}) = \dot{N}_{buff,H_2} t_{buff}, \tag{15}$$

and on this basis it is possible to calculate compression costs from Timmerhaus (Appendix D) and buffer tank installation costs (Hydrogen storage cost analysis final public report, 2013). The tank installation cost, actualized from 2013 and annualized, is $C_{H_2,tank} = 1.3\,€/\mathrm{mol}^{-1}_{H_2}$. The final cost, which also accounts for the compressor (the compression power being evaluated as in Equation (AE.CPR1.1, AE.CPR2.1), the cost as shown in Appendix D.3), reads:

$$C_{H_2,buff}(t_{buff}) = C_{H_2,tank}\, N_{H_2,buff}(t_{buff}) + C_{H_2,compressor,300\,bar}. \tag{16}$$

The estimate for the buffering costs given within this framework is shown in Fig. 12. The size of the buffer increases linearly with the loading time at a total power input of 50.5 MW. The cost of the compressor is independent on the tank size: it exclusively depends on the excess of power generated by the wind park, constant throughout the domain. The fixed cost of lithium batteries is significantly higher than the costs of the hydrogen buffering system.

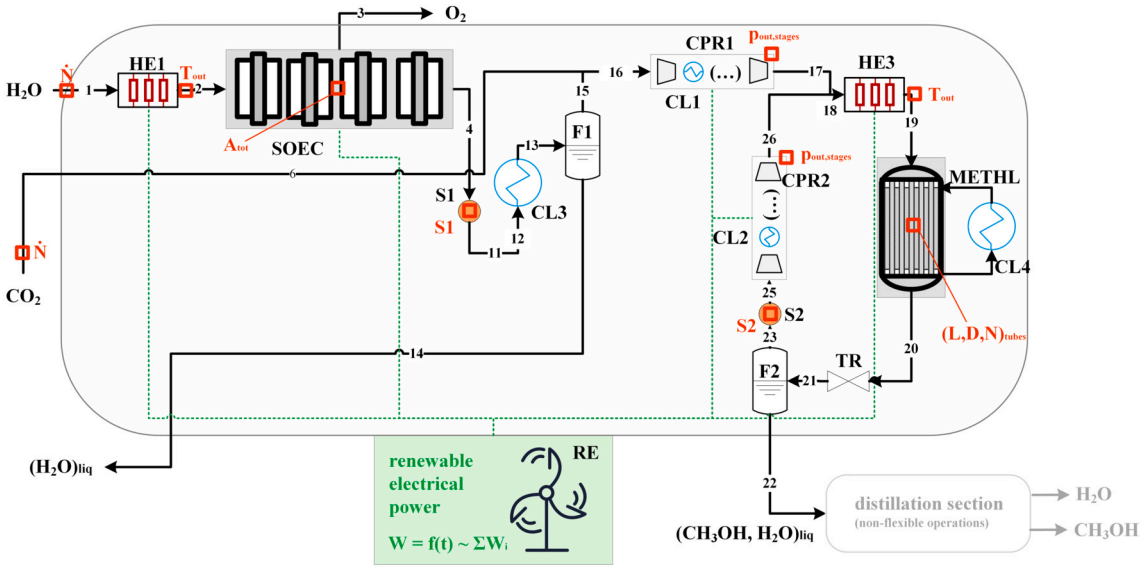

Fig. 6. Topological solution shared by the four optimization cases. The volume of RWGS is negligible, and thus is bypassed by the process flows. The recycle loop of METHL is closed.

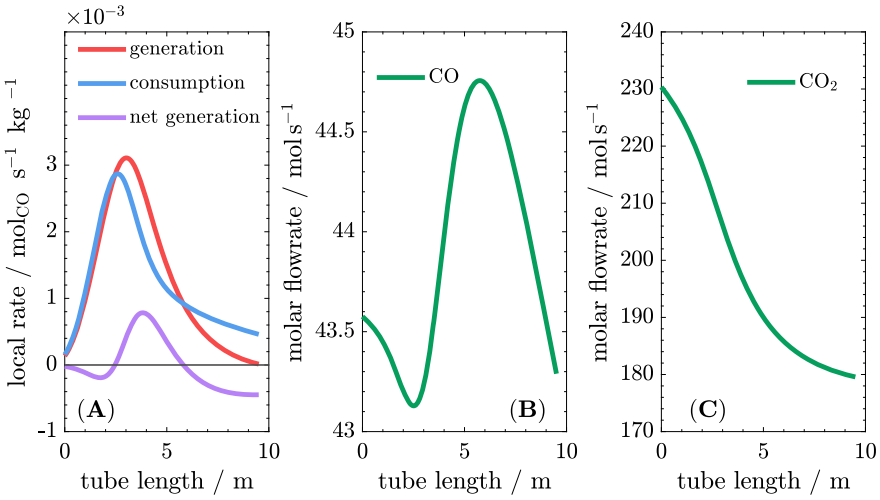

Fig. 7. (**A**) Rates of generation, consumption and net generation of carbon monoxide along the methanol synthesis reactor axis, per mass of catalyst (kg) for period 5 (highest load). In (**B**) and (**C**) the molar flowrate at period 5 for carbon monoxide and carbon dioxide, respectively.

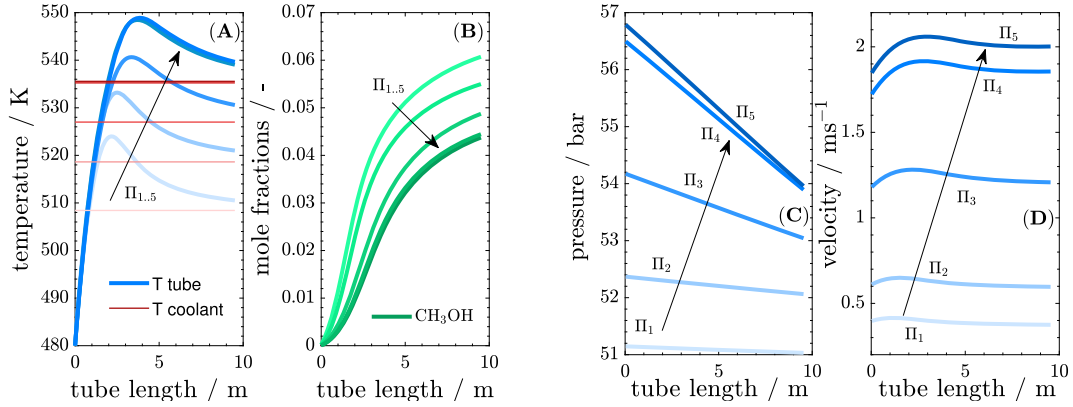

Fig. 8. Relevant profiles along the axial coordinate of METHL reactor for different periods for increasing loads, e.g., from Π_1 to Π_5: temperature and molar fraction profiles, (**A**) and (**B**), pressure and velocity profiles, (**C**) and (**D**). Figure (**A**) reports the cooling temperature level in red, constant along the axis (boiling water).

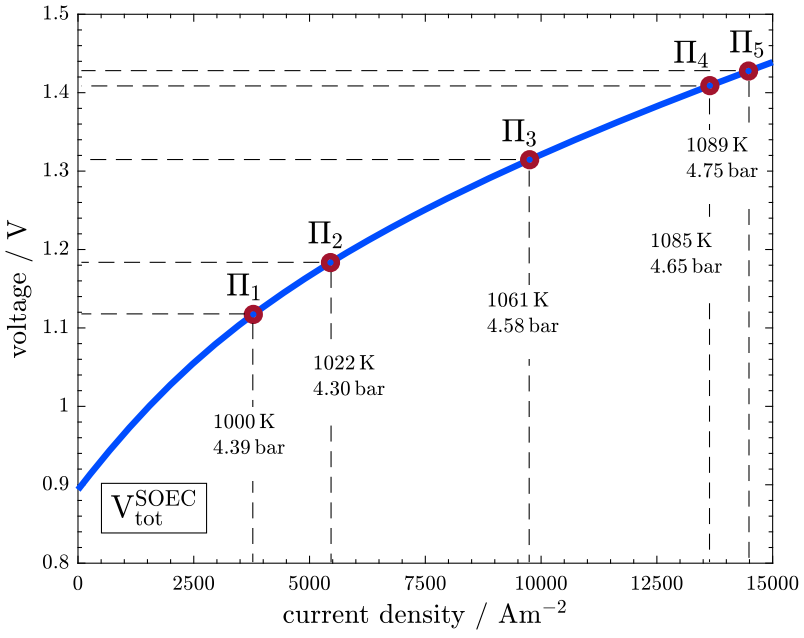

Fig. 9. This graph represents the current density and voltage resulting from NLP.FLEX. The points are labeled with the period identifier $\Pi_{i\in\{1,NP\}}$, the feed temperature and the operating pressure. The temperature drop is always equal to 30 K.

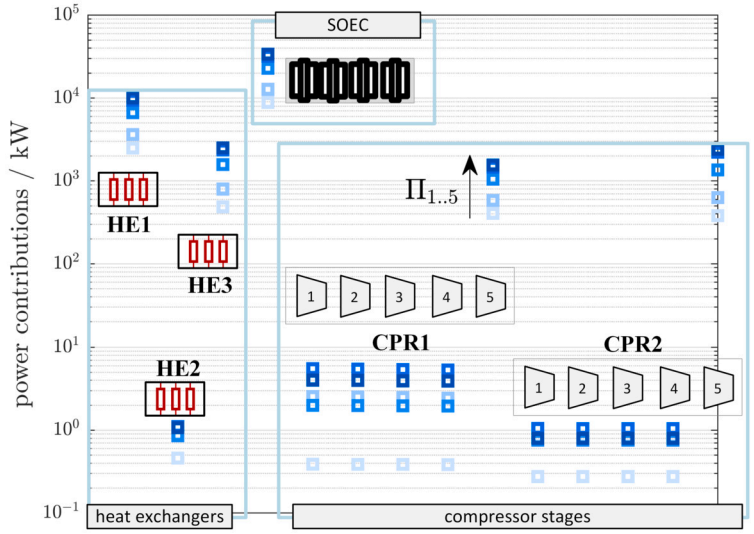

Fig. 10. Distribution of the power supplied within the plant, where the darker the blue, the larger the total power load to the plant, as illustrated by the arrow.

Given the trends in Fig. 12 and the solution of NLP.BUFF, it is possible to determine topology, investment cost and operating regime of the plant for CASE.BUFF (Tables 4 and 5). The Power-to-Methanol efficiency, 59.2%, lies between the efficiency at Π_2 (59.6%) and Π_3 (58.6%) of CASE.FLEX, reflecting the fact that the nominal load $\dot{W}_{tot}$ for CASE.BUFF, 23.5 MW, stays between the load at Π_2 (18.4 MW) and at Π_3 (33.5 MW) for CASE.FLEX.

The SOEC area (3904 m^2) is larger than the one identified in CASE.FLEX (2155 m^2), although operating temperature and pressure (1000 K, 4.31 bar) are comparable with those identified for Π_1 of CASE.FLEX (period at the lowest power supply, where SOEC temperature and pressure are 1000 K and 4.39 bar, respectively). In contrast, the volume of the METHL for CASE.BUFF (8.22 m^3) is smaller than for CASE.FLEX (10.5 m^3), as it does not have to withstand the large peaks of feed flowrate attained during the high load periods of CASE.FLEX, where pipes being too small in diameter would lead to excessive pressure drops. Most relevantly, these results offer the tool to ascertain whether buffering strategy F can be more profitable than steady-state plant operations, where either electricity or hydrogen is buffered (B.I and B.II in CASE.BUFF). This particular aspect is dealt with in the next Section.

6.2.1. *Contracting on the price of electricity can make total flexibility competitive*

The analysis is now restricted to a loading time comprised between 12 hr and 24 hr. Fig. 13 reports the profits for the three buffering scenarios B.I, B.II, F as a function of the loading time. Profits are denoted by superscript *, as they exclude all process elements that are assumed to be in common among the three buffering strategies, e.g., wind park, process fluids compressors (excluding the compressor for the storage of hydrogen), heat exchangers, coolers, piping etc. The linearly decreasing trends are determined by the increasing sizes of the buffering devices (B.I and B.II). The green lines (F) are independent on the abscissas and are identified by different letters (a, b, c), which are related to the red

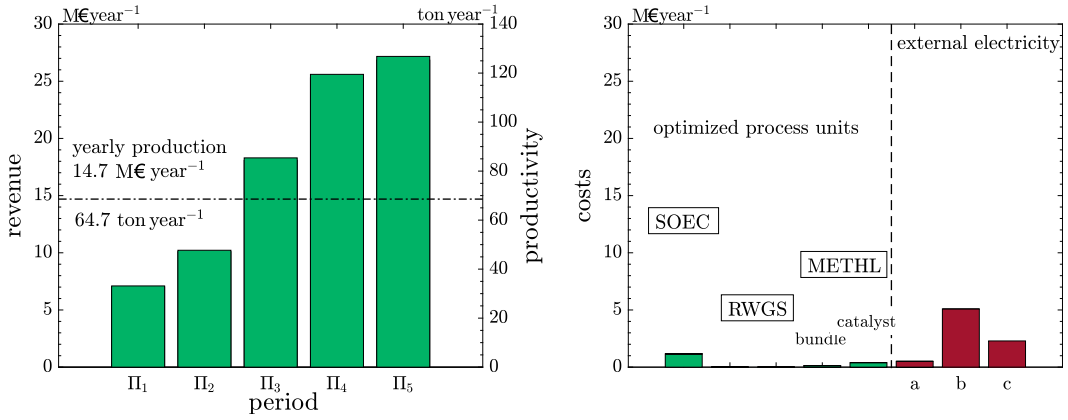

Fig. 11. (**A**) Revenues from the sale of methanol at 580 €ton^{-1} if each period were to be extended to the whole year. The results for the period and annual average values are shown as bars and dashed horizontal line, respectively; (**B**) annualized and actualized costs of the optimized unit operations (green bars), annual cost of external power supply to ensure stable plant operations over the period Π_1 for different scenarios of electricity prices: a (20 €MWh), b (200 €MWh), c (90 €MWh).

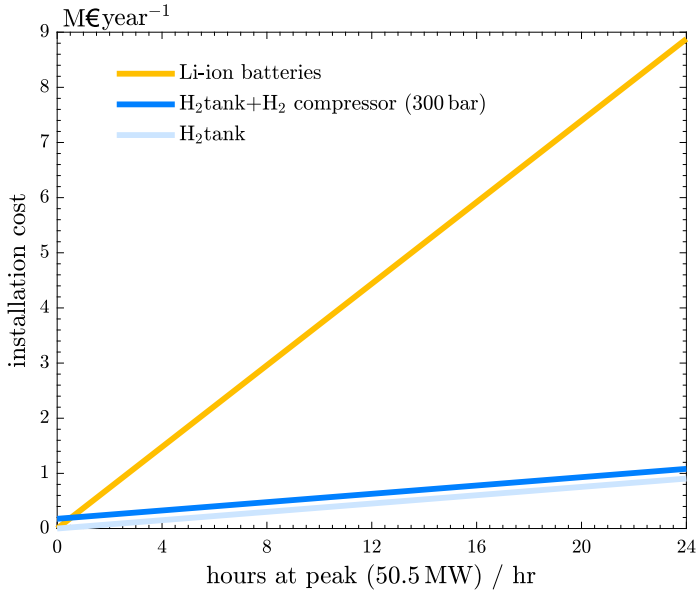

Fig. 12. Investment cost for buffering devices, calculated assuming the time (abscissa) spent by the wind park at 50.5 MW, 27 MW higher than the power absorbed by the methanol plant.

bars in Fig. 11 (B). These represent three prices of electricity integrated from external sources (grid) to support plant operations at period Π_1 for flexible plant operations (F). If the external electricity is supplied from a delocalized renewable source at 20 €MWh^{-1}, flexible operations result in a more profitable process candidate. Nevertheless, this price is typical of renewable power plants allocated in the vicinity of the plant, which are therefore not dependent on the grid infrastructure, which might appear as an overly optimistic perspective. As for grid electricity, typical prices can reach and exceed 200 €MWh^{-1}. In this case, it is clear that the profits from a strategy based on total flexibility are lower than those from buffering hydrogen, although this margin decreases as the buffer size increases. In a third framework c, the maximum electricity price that the company is willing to pay can be outlined against negotiations with the external electricity supplier, so that the flexible approach can be at least as profitable as strategy B.II. For this case-study, this price is 90 €MWh^{-1} for 12 hr at the peak load.

6.3. Results for CASE.EFF: maximum efficiency for B.I and B.II, no heat integration

The maximization of Power-to-Methanol efficiency for a plant operated at 23.5 MW – Objective (OBJ.EFF.SP). – results in a gain of 3% over the corresponding value for CASE.BUFF at a significantly higher investment cost: the sum of actualized and annualized costs for the optimized units, i.e., SOEC, RWGS, METHL, is 4.6 times higher than in CASE.BUFF, which makes these results inapplicable.

6.4. Results for CASE.FLEX.HI: maximum profit with heat integration

Heat integration results in a higher Power-to-Methanol efficiency. Fig. 14 (A) highlights the period-related gain in efficiency after heat integration: its mean annual value is almost 7% higher than the corresponding value obtained without heat integration (CASE.FLEX). Heat integration also results in a higher cost of the optimized units (SOEC, METHL), although revenues are largely improved. Consequently, the plant configuration with heat integration is more profitable, as shown in the comparison in Fig. 14 (B).

7. Estimated energy requirements

As reported in the former Section 2.3, feedstock generation and conditioning is not incorporated in the mathematical optimization. For this reason, the following calculations assume a linear trend of the energy consumption retrieved from the literature with the flowrate of water

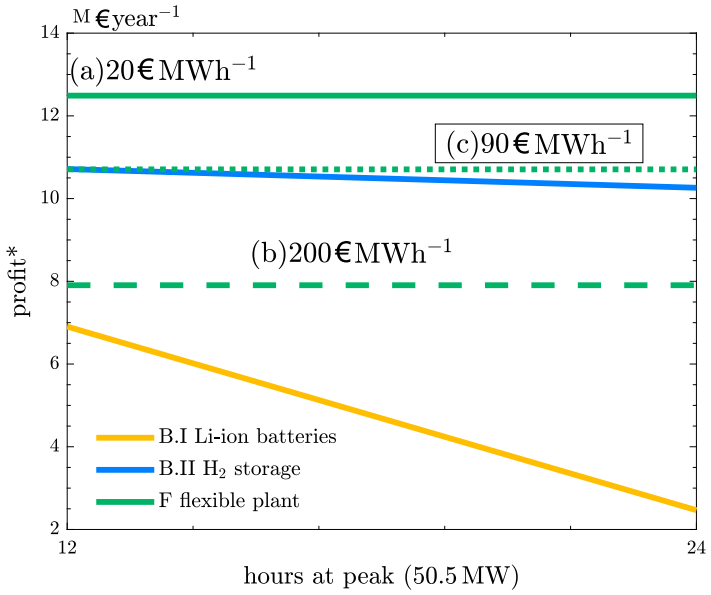

Fig. 13. Profit* versus loading time for the three buffering scenarios. The asterisk indicates that these values are built upon the optimized units (SOEC, RWGS, METHL), whereas all other process elements preserve their sizes and costs in the different cases. Profits for lithium batteries and hydrogen storage are inversely proportional to the size of the buffers. Profitability of the flexible setup F is highly dependent on the price of external electricity, denoted with letters (a,b,c) as commented in Fig. 11.

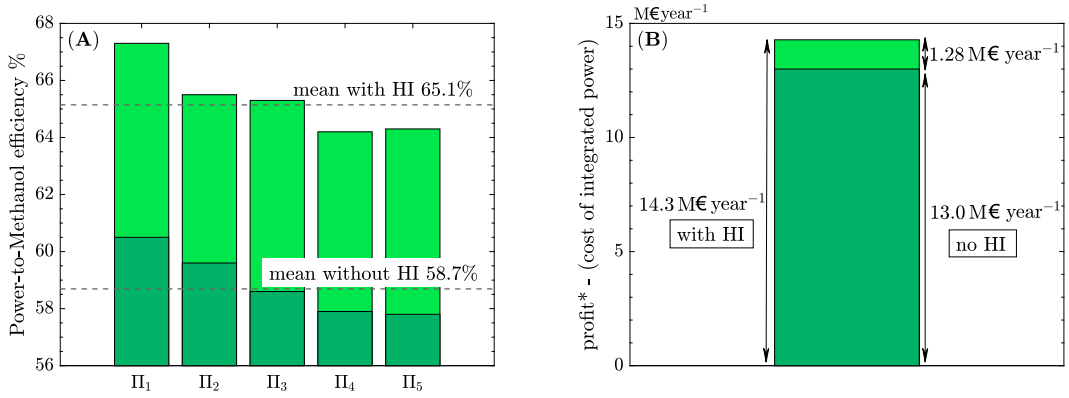

Fig. 14. (**A**) Period-related Power-to-Methanol efficiency in light and dark green with and without heat integration (HI), respectively. Dashed lines depict the annual mean values of efficiency; (**B**) comparison between pseudo-profits with and without heat integration, not accounting for the cost of the external electricity supply at Π_1, which is the same.

and carbon dioxide, respectively: the energy consumption in the flexible case is directly proportional to their flowrate at the period with the highest load. It is then assumed that the size of these technologies is fixed for different flexibility scenarios, and does not have an impact on their comparative analysis. Nevertheless, this aspect should be proven in future studies by including such unit operations in the optimization framework.

7.1. Seawater desalination and carbon capture

The flexible methanol plant without heat integration (CASE.BUFF) processes a annual flowrate of purified water of $\sum_{j\in\{1,NP\}} \omega_j \dot{N}_{j,H_2O} = 66.1\,\mathrm{mol\,s^{-1}}$. The seawater desalination system must be stabilized accordingly by means of dedicated batteries in order to preserve the provided flowrate in spite of the fluctuations in renewable power. Accounting for seawater losses (40%), salinity (3.5%) and density ($1028\,\mathrm{kg\,m^{-3}}$), the total annual volumetric flowrate of processed seawater amounts to $1.998\times10^{-3}\,\mathrm{m^3\,s^{-1}}$. Consequently, a RO desalination device requiring $6\,\mathrm{kWh\,m^{-3}_{seawater}}$ has to adsorb 43.2 kW and to be dimensioned accordingly. On the contrary, if flexibly operated (CASE.FLEX), RO would have to withstand a power peak input of 90 kW, relatable with the maximum water intake for the flexible methanol plant ($138\,\mathrm{mol\,s^{-1}}$).

A S-DAC operated to supply a constant feed flowrate of carbon dioxide to the optimal methanol plant operated at constant load (CASE.BUFF) is supplied with 1.4 MW and 4.4 MW electrical and thermal power duty respectively, supplying $21.9\,\mathrm{mol_{CO_2}\,s^{-1}}$. Amine scrubbing (MEA) of flue gas, reportedly an energy intensive state-of-the-art process, requires half the thermal demand (2.4 MW). Assuming that no heat integration supports the thermal duty of S-DAC and CC, and that heat is provided by combustion of methane (lower heating value of $800\,\mathrm{kJ\,mol^{-1}}$), the percentage of CO_2 generated compared to that introduced in the synthesis process is 25% (S-DAC) and 14% (CC). Clearly, flue gases from CC can be recirculated back to its own feed, whereas DAC would release them directly into the atmosphere, although its net CO_2 emission is still negative. In the flexible case (CASE.FLEX), $45.9\,\mathrm{mol_{CO_2}\,s^{-1}}$ (highest load), are supplied to the methanol plant. Electrical and thermal duty of S-DAC are 2.9 MW and 9.2 MW, the reboiler duty for CC amounts to 5 MW.

All this considered, the renewable power plant must ensure the production level by means of additional 0.09 MW for water desalina-

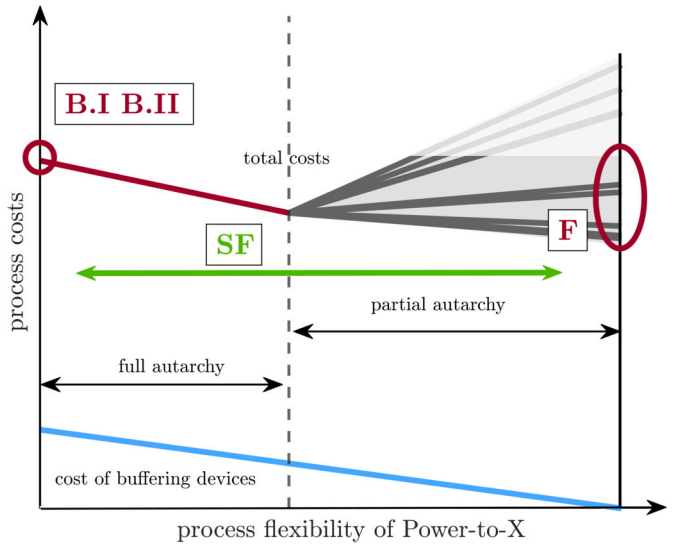

Fig. 15. Process costs as a function of process flexibility for a generic Power-to-X system: flexible regime (F), Li-ion batteries and hydrogen buffering (B.I, B.II), semi-flexible plant (SF). The red line identifies costs in a regime of energy autarchy, where the renewable power is entirely produced and consumed within the chemical plant. Further to the right, the plant requires an external power input, as renewable power is not sufficient to support feasible operations. The costs of buffering devices are reported in blue.

tion and 2.9 MW if S-DAC is implemented for the largest period of CASE.FLEX at nominal regime, a total of 3 MW of additional electricity on top of the 50 MW already assumed for the methanol synthesis plant being optimized. This requirement can be covered by installation of an additional wind turbine. Furthermore, heat integration with the hot cooling water of the methanol synthesis reactor can reduce the thermal duty for the supplementary DAC or CC system due to their low regeneration temperatures.

7.2. Distillation

A shortcut distillation column is sufficient to estimate the thermal duty at the distillation section in the downstream of the methanol synthesis process. For this purpose, a DSTWU model (Aspen plus®) is fed with the methanol/water mixture in stream 23 (CASE.BUFF, 22.3 $\mathrm{mol_{H_2O}\,s^{-1}}$, 21.8 $\mathrm{mol_{CH_3OH}\,s^{-1}}$). A purity of 98.5% and a recovery of 99% can thus be determined by a column with 28 stages operated at ambient pressure and a reflux ratio of 1.3 and with total condensation. Thermal duties at reboiler and condenser are 2.8 MW and −1.93 MW at 65 °C and 90 °C, respectively. The low temperature at the reboiler may favor heat integration options with other process lines in the methanol synthesis section of the plant.

8. Discussion

In the former section, results from the case of total flexibility (CASE.FLEX) were compared with buffering of electricity and hydrogen for steady-state operations (CASE.BUFF and CASE.EFF) due to the fact that fixed costs decrease proportionally with the size of buffering devices. As shown, negotiating on the price of the integrating external electricity supply for the low-load period Π_1 is the key to allow for a potentially competitive flexible process which does not resort to buffering devices. The relation between costs of different buffering strategies can be qualitatively visualized in Fig. 15, where total and buffering costs of a generic P2X process are functions of the extent of its flexibility.

At the origin of the abscissa, the process is operated at a nominal load throughout the year with large buffers (strategies B.I and B.II) in full energy autarchy, i.e., solely relying on the renewable power produced within the plant limits. Conversely, at the end of the abscissa, buffering devices are absent and the total cost is determined by the price of the complementary external electricity supply (strategy F). From the comparison with the single-period results in B.I and B.II, the maximum electricity price which plant owners should aim for during negotiations for a flexible, non buffered plant (F) is identified, as highlighted earlier in Section 6.2.1. If such price were not to be attained, intermediate solutions with small buffering devices and semi-flexible operations may be selected. This allows to run the plant with more expensive external electricity integrated at low-load (period Π_1), in partial energy autarchy and semi-flexible plant operations (denoted in the figure by a green arrow and labeled as strategy SF). The design of the P2X system should then be repeated for a reduced feasibility gap, implementing once again the multi-period design optimization approach highlighted in this article.

9. Summary, conclusions and outlook

A novel multi-period optimization application is proposed to design and operate a flexible, completely electrified plant for the production of methanol from in-house generated fluctuating wind electricity. In contrast to the prevailing literature in the field of multi-period optimization of P2X systems, distributed models and detailed non-ideal gas relations constrain the nonlinear programs (NLPs), which thus allow for a high fidelity representation of the system and ensure the feasibility of the identified design solutions. The conversion steps involved are SOEC-based water electrolysis, carbon monoxide generation in a reverse water-gas shift adiabatic reactor, and the methanol synthesis reactor. Side reactions are included in the kinetic models. In addition, two aspects lead to significant consequences in the decision-making: the electrification of the entire process and the general purpose of P2X systems, which is to store fluctuating energy in chemical bounds without allowing for surplus energy. These key aspects introduce a relevant extent of interconnection between process units: they cannot be optimized separately prior to overall plant evaluations. Therefore, all process units in the plant are simultaneously incorporated for the NLP optimization of design and operating conditions. At the same time, process constraints, operation variables and states are replicated for a finite number of periods, which approximate the power curve of the renewable power plant on an annual basis.

By means of this effective design tool, the present study explores the profound implications that the intermittent renewable power introduces in the analysis and selection of suitable process candidates. Firstly, a highly flexible plant designed in compliance with multi-period optimization results can compensate for the absence of buffering devices, provided that at low loads the process is supplied with external power. In terms of topology, the RWGS reactor is essentially excluded by the optimizer as it is assigned a negligible volume, although the presence of carbon monoxide in the recycle loop is beneficial for the methanol reactor kinetics. SOEC operations and steam generation at its feed determine the highest power demand. Consequently, profitability and Power-to-Methanol efficiency are increased via heat integration. The resulting process design represents the most cost attractive and technically feasible compromise across periods. This optimization solution provides a valid benchmark against which single-period optimization solutions are compared. At this yearly-averaged power supply, the plant was designed and operated. Large buffers for the storage of electricity and hydrogen are assumed. Results reveal that the flexible, non-buffered plant can be competitive if the price of externally integrated power is limited by negotiations. Intermediate process solutions with small buffers and moderate flexibility can offer more profitable process candidates, an interesting point to be analyzed in future applications of this methodological approach.

Although the current implementation in 5 periods allows for an agile workflow, which enables the NLP to be constructed by the solver in a reasonable time (15 min), future studies may attempt approaches for a

finer discretization of the power curve reported in Fig. 4 without losing in modeling accuracy, for instance, by model order reduction (MOR). Moreover, Section 2 prescribe nominal flowrates and energy intakes for the downstream (distillation) of the methanol plant. Thus, the analysis and design of this system can be decoupled from the design of the flexible methanol plant. This approach can be generalized as follows: a large process system can be divided into subsections capable of withstanding different extents of flexibility. The maximum extent of flexibility is subject to the technical limitations of the single unit operation. Future contributions shall generalize and exemplify this approach, e.g., by setting lower and upper thresholds on admissible flowrates to the distillation unit, then included in the final NLP. Furthermore, operation variables resulting from the multi-period solution constitute set-point values which the plant attains to ensure optimal operations for the given period, i.e., power load. In future studies, the dynamic effects between consecutive operating regimes shall be identified: an optimal control approach based on dynamic models should be formulated and solved in order to identify the fastest transition procedure and control values.

CRediT authorship contribution statement

Andrea Maggi conceptualized the case study in detail, formulated the modeling assumptions on a unit operation level and on a plant level, both in the flexible and steady operation scenarios, collected and tuned cost functions, formulated preliminary simulations and final optimizations. A.M. analyzed collected and analyzed the results and formulated the conclusions. A.M. wrote the manuscript and generated the figures.

Jens Bremer contributed with A.M. to the conceptualization, the formulation of optimization scenarios and the analysis of results in his mentoring role. J.B. also suggested the use of CasADi for optimization and shared his expertise in the field of optimization. J.B. proofread the manuscript and recommended the first internal revision of the draft.

Kai Sundmacher advised A.M. in the selection of the research direction and of the case study on a high level. K.S. revised the entire manuscript before submission.

Declaration of competing interest

The authors declare that they have no known competing financial interests or personal relationships that could have appeared to influence the work reported in this paper.

Data availability

Data will be made available on request.

Funding

K.S. organized funding of the whole project from the core budget of the Max Planck Institute for Dynamics of Complex Technical Systems, Magdeburg (Germany).

Appendix A. List of symbols

A list of symbols is reported in Table A.6. The symbols adopted in Appendix B and Appendix C are given here only when necessary for clarity. Indices are reported together with the symbols.

Appendix B. Supplementary section - wind park parametrization

B.1. Wind turbine power curve

Data for the definition of the power curve generated by the wind park are reported in Table B.7 and retrieved the technical sheet of a 2.1 MW wind turbine (GmbH, 2012).

B.2. Monthly wind velocity

The monthly average wind velocity in Magdeburg is retrieved from Weather Spark (2022) and reported in Table B.8.

Appendix C. Supplementary section - system models parametrization

C.1. Modeling of SOEC

Factors in Equation (AE.SOEC.2), (AE.SOEC.3):

$$\Lambda_1 = \frac{\zeta_{\mathrm{av,H_2,TPB}}}{\zeta_{\mathrm{av,H_2}}}, \quad \Lambda_2 = \frac{\mathcal{E}_{\mathrm{faraday}}}{R_{\mathrm{gas}} T_{\mathrm{av}}}, \quad \Lambda_3 = \frac{\zeta_{\mathrm{av,H_2O,TPB}}}{\zeta_{\mathrm{av,H_2O}}}, \quad \Lambda_4 = \frac{-\mathcal{E}_{\mathrm{faraday}}}{R_{\mathrm{gas}} T_{\mathrm{av}}}, \tag{C.1}$$

where subscript "av" denotes an average value between inlet and outlet of SOEC, R_{gas} the universal gas constant ($8.314\,\mathrm{J\,mol^{-1}\,K^{-1}}$), $\mathcal{E}_{\mathrm{faraday}}$ the Faraday constant, subscript "TBP" denotes the concentration at the triple phase boundary. Mole fractions $\zeta_{\mathrm{av},i\in\{\mathrm{H_2,H_2O}\}}$ at the cathode read:

$$\zeta_{\mathrm{av,H_2}} = \frac{\dot{N}_{\mathrm{av,H_2}}}{\dot{N}_{\mathrm{av,H_2}} + \dot{N}_{\mathrm{av,H_2O}}}, \quad \zeta_{\mathrm{av,H_2O}} = \frac{\dot{N}_{\mathrm{av,H_2O}}}{\dot{N}_{\mathrm{av,H_2}} + \dot{N}_{\mathrm{av,H_2O}}}. \tag{C.2}$$

Other terms appearing in Equation (C.1) are expanded here:

$$\zeta_{\mathrm{av,H_2,TPB}} = \zeta_{\mathrm{av,H_2}} + \frac{\tau_{\mathrm{cat}}}{2\mathcal{E}_{\mathrm{faraday}} D_{\mathrm{eff,cat}} C_{\mathrm{tot,av}}} i_{\mathrm{SOEC}}, \tag{C.3}$$

$$\zeta_{\mathrm{av,H_2O,TPB}} = \zeta_{\mathrm{av,H_2O}} - \frac{\tau_{\mathrm{cat}}}{2\mathcal{E}_{\mathrm{faraday}} D_{\mathrm{eff,cat}} C_{\mathrm{tot,av}}} i_{\mathrm{SOEC}},$$

where $C_{\mathrm{tot,av}}$ is the ideal gas average concentration between inlet and outlet of SOEC, τ_{cat} is the cathode thickness (500×10^{-6} m), $D_{\mathrm{eff,cat}}$ is the average effective diffusivity coefficient of the cathode ($36.6\times10^{-6}\,\mathrm{m^{-2}\,s^{-1}}$).

The total voltage is given by the sum of reversible and irreversible contributions.

$$V_{\mathrm{tot}}^{\mathrm{SOEC}} = V_{\mathrm{nernst}} + V_{\mathrm{ohm}} + V_{\mathrm{conc}} + V_{\mathrm{act,cat}} + V_{\mathrm{act,an}}, \tag{C.4}$$

$$V_{\mathrm{nernst}} = -\frac{g^0_{\mathrm{f,H_2O}}(T_{\mathrm{in}})}{2\mathcal{E}_{\mathrm{faraday}}} - R_{\mathrm{gas}} \frac{T_{\mathrm{av}}}{2\mathcal{E}_{\mathrm{faraday}}} \ln\left(\frac{\zeta_{\mathrm{av,H_2O}}}{\zeta_{\mathrm{av,H_2}} \zeta_{\mathrm{av,O_2}}^{0.5}}\right),$$

$$V_{\mathrm{ohm}} = i_{\mathrm{SOEC}} \left(\frac{\tau_{\mathrm{cat}}}{\sigma_{\mathrm{cat}}} + \frac{\tau_{\mathrm{el}}}{\sigma_{\mathrm{el}}} + \frac{\tau_{\mathrm{an}}}{\sigma_{\mathrm{an}}}\right),$$

$$V_{\mathrm{conc}} = R_{\mathrm{gas}} \frac{T_{\mathrm{av}}}{2\mathcal{E}_{\mathrm{faraday}}} \ln\left(\zeta_{\mathrm{av,H_2,TPB}} \frac{\zeta_{\mathrm{av,H_2O}}}{\zeta_{\mathrm{av,H_2}} \zeta_{\mathrm{av,H_2O,TPB}}}\right)$$

whereas $V_{\mathrm{act,cat}}$ and $V_{\mathrm{act,an}}$ are implicit dependencies of other variables and must be calculated as NLP constraints, (AE.SOEC.2) and (AE.SOEC.3). In Equation (C.4); T_{av} is the average temperature between the inlet and outlet of SOEC, $g^0_{\mathrm{f,H_2O}}(T_{\mathrm{in}})$ is the Gibbs free energy of formation of water at the feed temperature to SOEC; $\zeta_{\mathrm{av,O_2}}$ is the mole fraction of oxygen in the sweep gas (pure, thus of value one); $\zeta_{\mathrm{av,H_2O}}$ and $\zeta_{\mathrm{av,H_2}}$ are average component compositions at the cathode (see Equation (C.2)); τ_{cat}, τ_{el} and τ_{an} are the cathode, the electrolyte and the anode thickness (500×10^{-6} m, 20×10^{-6} m, 50×10^{-6} m, respectively). The cathode electric conductivity, the electrolyte ionic conductivity and the anode electric conductivity are denoted by σ_{cat}, σ_{el} and σ_{an} ($80\times10^3\,\Omega^{-1}\,\mathrm{m^{-1}}$, $33400\exp(-10300/T_{\mathrm{S}})\,\Omega^{-1}\,\mathrm{m^{-1}}$, $8400\,\Omega^{-1}\,\mathrm{m^{-1}}$, respectively).

C.2. Modeling of flash separator F2 (methanol recycle loop)

Mixture fugacity coefficient $\Phi_{\alpha,\mathrm{phase}\in\{\mathrm{vap,liq}\}}$ for condensable components ($\alpha \in \{\mathrm{H_2O, CH_3OH}\}$) in liquid and vapor phase read:

Table A.6
List of symbols.

Symbol	Description	Unit (SI)
α_{eff}, α_{w}	heat transfer coefficient (effective, wall)	$\text{W m}^{-2}\text{ K}^{-1}$
$\alpha_{\text{mix,phase}}$, $\alpha_{\alpha,k}$	EOS cubic coefficient (mixture, pure component α at node k)	-
$\beta_{\text{mix,phase}}$, $\beta_{\alpha,k}$	EOS cubic coefficient (mixture, pure component α at node k)	-
$\gamma_{\text{mix,phase}}$, $\gamma_{\alpha,k}$	EOS cubic coefficient (mixture, pure component α at node k)	-
ε	void fraction in packed-bed reactors	$\text{m}^3_{\text{gas}}\text{ m}^{-3}_{\text{reactor}}$
ζ_α	molar fraction of component α	-
$\eta_{\text{PtCH}_3\text{OH}}$	Power-to-Methanol efficiency based on LHV	-
κ	isentropic coefficient	-
λ_{mix}, λ_{bed}, λ_{cat}	thermal conductivity (gas mixture, bed, catalyst)	$\text{W m}^{-1}\text{K}^{-1}$
Λ_{r}	effective radial thermal conductivity	$\text{W m}^{-1}\text{K}^{-1}$
$\Lambda_{(1,2,3,4)}$	lumping factors for SOEC models	-
μ_{mix}	average viscosity in bulk phase	Pa s^{-1}
$\nu_{\alpha,k}$	stoichiometric coefficient of component α in reaction k	-
ξ	ratio between vapor and feed molar flowrate (flash)	-
(π)	superscript denoting variables shared across periods	-
Π_i	i-th period	-
ρ_{cat}, ρ_{gas}	density (catalyst, gas)	$\text{kg}_{\text{cat}}\text{ m}^{-3}_{\text{cat}}$
σ_α	(overall) molar generation rate for single component α	$\text{mol kg}^{-1}_{\text{cat}}\text{ s}^{-1}$
ω_i	probability of period i	-
$a_{\text{mix,phase}}$, $a_{i,j,\text{phase}}$, $a_{\alpha,\text{phase}}$	EOS parameter (mixture, binary interaction of pair i-j, pure component α)	-
A	kinetic pre-exponential factor	various
AE, **AE**	algebraic equation (single, set)	various
$A_{\text{EOS,phase}}$, $A_{\text{EOS},\alpha,\text{k}}$	EOS parameter (mixture, pure component α)	-
$A^{(\pi)}_{\text{SOEC}}$, A_{cross}	area SOEC, cross sectional area reactor	m^2
$b_{\text{mix,phase}}$, $b_{i,j,\text{phase}}$, $b_{\alpha,\text{phase}}$	EOS parameter (mixture, binary interaction of pair i-j, pure component α)	-
$B_{\text{EOS,phase}}$, $B_{\text{EOS},\alpha,\text{k}}$	EOS parameter (mixture, pure)	-
$C^{(\pi)}_i$, $\dot{C}^{(\pi)}_i$, $\dot{C}_{22,\text{CH}_3\text{OH},\Pi_j}$	cost of unit i (absolute, annualized), annualized revenue at period j	€, $€\,\text{year}^{-1}$
C_{gas}	gas concentration (for reactors, in bulk phase)	$\text{mol}_{\text{gas}}\text{ m}^{-3}$
$\tilde{C}^{\text{gas}}_{\text{p,gas}}$, $\tilde{C}_{\text{p},\alpha}$	molar specific heat at constant pressure (bulk, component α)	$\text{J mol}^{-1}\text{ K}^{-1}$
DE, **DE**	differential equation (single, set)	various
$D^{(\pi)}_{\text{cat},k}$, $D^{(\pi)}_{\text{T},k}$	diameter of reactor k (catalyst, reactor tube)	m
E	kinetic activation energy	J mol^{-1}
$\dot{H}$, $\dot{H}_{\text{in/out}}$	flow enthalpy (generic, inlet/outlet)	J s^{-1}
$\tilde{H}_\alpha$, $\tilde{H}_{i,\alpha}$	molar enthalpy of component α (generic, i-th stream)	J mol^{-1}
ΔH_{R}, $\Delta H_{\text{ev}}(298\,\text{K})$	enthalpy of reaction, latent heat of vaporization	J
i_{SOEC}, $i_{\text{av,cat/an}}$	current density SOEC (total, exchange cathode/anode)	A m^{-2}
k_i	kinetic constant of reaction i	various
K_α	adsorption constant of species α	various
$K_{\text{eq},i}$	equilibrium constant of reaction i	-
$\mathbf{LBX}^{(\pi)}$, $\mathbf{UBX}^{(\pi)}$	vector of bounds to design variables (lower, upper)	various
$\widetilde{\mathbf{LBX}}$, $\widetilde{\mathbf{UBX}}$	vector of bounds to operation variables (lower, upper)	various
$L^{(\pi)}_{\text{T},k}$	tubes length of reactor k	m
$\text{LHV}_{\text{CH}_3\text{OH}}$	low heating value of methanol	J mol^{-1}
$\dot{N}_{\text{tot},i}$, $\dot{N}_{i,\alpha}$	molar flowrate (total i-th stream, component α in stream i)	mol s^{-1}
NP	number of periods	-
M_α	molecular weight of component α	g mol^{-1}
$N^{(\pi)}_{\text{T,METHL}}$	number of tubes in the methanol reactor	-
p, $p_{\text{in/out},k}$	total pressure (generic, inlet or outlet unit k)	Pa
$\dot{Q}_{\text{CL}}$	Cold duty demand for the generic condenser CL	W
R_i	molar reaction rate for reaction i	$\text{mol kg}^{-1}_{\text{cat}}\text{ s}^{-1}$
R_{gas}	universal gas constant	$\text{J mol}^{-1}\text{ K}^{-1}$
S	split factor	-
t	time	s
T, $T_{\text{in/out},k}$, T_{cool}	temperature (generic, inlet or outlet unit k, coolant METHL)	K
U	overall heat transfer coefficient	$\text{W m}^{-2}\text{ K}^{-1}$
v, v_{wind}	interstitial velocity (reactor), wind velocity	m s^{-1}
$V_{\text{tot,SOEC}}$, V_i	SOEC voltage (total, single i-th contribution)	V
$\dot{W}_{\text{tot}}(t)$, $\dot{W}_{\text{tot},j}$, $\dot{W}_{\text{k}}$	power input (total at time t, total - averaged at period j, to unit k)	W
$\boldsymbol{x}^{(\pi)}$	optimization variables shared across periods (vector)	-
$\tilde{\boldsymbol{x}}$, $\overline{\tilde{\boldsymbol{x}}}$	optimization variables not shared across periods (vector)	-
z	axial coordinate	m
$Z_{\text{mix,phase}}$, $Z_{\alpha,\text{phase},k}$	compressibility factor (mixture, component α at point k)	-
CL	cooler	-
CPR	train of adiabatic compressors	-
DEN	denominator in the rates of reaction	-
F	flash separator	-
HE	electrical heat exchanger	-
METHL	methanol reactor	-
MIX	mixer	-
RE	renewable energy (wind power)	-
RWGS	reverse water-gas shift reactor	-
S	splitter	-
SOEC	solid-oxide electrolyzer	-
TR	throttle valve	-

Table B.7
Data are retrieved from the technical sheet of a wind turbine (2.1 MW S95 Sulzon).

$m\,s^{-1}$	3.0	3.5	4.0	4.5	5.0	5.5	6.0	6.5	7.0	7.5
kW	0.0	2.6	52.3	122.5	206.4	304.0	414.9	539.5	683.1	839.2
$m\,s^{-1}$	8.0	8.5	9.0	9.5	10.0	10.5	11.0	11.5	12.0	12.5
kW	1010.0	1197.1	1393.2	1592.4	1787.7	1931.2	2016.3	2068.3	2096.4	2109.2
$m\,s^{-1}$	13.0	13.5	14.0	14.5	15.0	15.5	16.0	16.5	17.0	17.5
kW	2114	2116.5	2116.2	2116	2115.8	2115	2114.5	2114.2	2113.87	2112.2
$m\,s^{-1}$	18.0	18.5	19.0	19.5	20.0	20.5	21.0	21.5	22.0	22.5
kW	2111.2	2110.5	2109.8	2105.5	2104.4	2103.2	2102	2096.4	2092.8	2091.2
$m\,s^{-1}$	23.0	23.5	24.0	24.5	25.0					
kW	2089.7	2088.2	2086.6	2084.9	2084.9					

Table B.8
Average monthly wind velocities in Magdeburg, Germany.

$km\,hr^{-1}$	19.2	18.5	17.7	15.3	14.2	14.1	14.0	13.9	14.9	15.9	16.9	18.3

Table C.9
List of parameters for RWGS kinetics: pre-exponential and activation energies.

$A(k_i)$ and $A(K_i)$	Value	unit (SI)	$E(k_i)$ and $E(K_i)$	Value	unit (SI)
$A(k_{SR})$	1.17×10^{12}	$kmol\,bar^{0.5}\,kg_{cat}^{-1}\,s^{-1}$	$E(k_{SR})$	2.40×10^{5}	
$A(k_{WGS})$	5.43×10^{2}	$kmol\,bar^{-1}\,kg_{cat}^{-1}\,s^{-1}$	$E(k_{WGS})$	6.71×10^{4}	
$A(k_{RMETH})$	2.83×10^{11}	$kmol\,bar^{0.5}\,kg_{cat}^{-1}\,s^{-1}$	$E(k_{RMETH})$	2.44×10^{5}	
$A(K_{CH_4})$	6.65×10^{-4}	bar^{-1}	$E(K_{CH_4})$	-3.83×10^{4}	$J\,mol^{-1}$
$A(K_{H_2O})$	1.75×10^{5}	–	$E(K_{H_2O})$	8.87×10^{4}	
$A(K_{CO})$	8.23×10^{-5}	bar^{-1}	$E(K_{CO})$	-7.07×10^{4}	
$A(K_{H_2})$	6.12×10^{-9}	bar^{-1}	$E(K_{H_2})$	-8.29×10^{4}	

$$\Phi_{\alpha,\text{phase}} = \exp\left(\frac{b_{\alpha,\text{phase}}}{b_{\text{mix,phase}}}\left(Z_{\text{mix,phase}}-1\right)-\log\left(\left|Z_{\text{mix,phase}}-B_{\text{EOS,phase}}\right|\right)-..\right. \tag{C.5}$$
$$\left.\frac{A_{\text{EOS,phase}}}{B_{\text{EOS,phase}}}\left(2\cdot\sqrt{\left(\frac{a_{\alpha,\text{phase}}}{a_{\text{mix,phase}}}\right)}\right)-\frac{b_{\alpha,\text{phase}}}{b_{\text{mix,phase}}}\log\left(1+\frac{B_{\text{EOS,phase}}}{Z_{\text{mix,phase}}}\right)\right).$$

Coefficients for the cubic Equations (AE.F2.2), (AE.F2.3) (flash in the methanol reactor loop) read:

$$\alpha_{\text{mix,phase}} = -1, \tag{C.6}$$
$$\beta_{\text{mix,phase}} = A_{\text{EOS,phase}} - B_{\text{EOS,phase}} - B_{\text{EOS,phase}}^2,$$
$$\gamma_{\text{mix,phase}} = -A_{\text{EOS,phase}}\,B_{\text{EOS,phase}},$$

where

$$A_{\text{EOS,phase}} = a_{\text{mix,phase}}\frac{p}{\left(R_{\text{gas}}T\right)^2}, \tag{C.7}$$
$$B_{\text{EOS,phase}} = b_{\text{mix,phase}}\frac{p}{\left(R_{\text{gas}}T\right)},$$

and, introducing two new indices for components in the mixture i and j to explore binary interactions,

$$a_{\text{mix,phase}} = \sum_{i\in I}\sum_{j\in J}\zeta_{i,j,\text{phase}}\,a_{i,j,\text{phase}}, \tag{C.8}$$
$$b_{\text{mix,phase}} = \sum_{i\in I}\zeta_{i,\text{phase}}\,b_{i,\text{phase}},$$

and

$$a_{i,j,\text{phase}} = \sqrt{a_{i,\text{phase}}\,a_{j,\text{phase}}}\left(1-K_{i,j}\right), \tag{C.9}$$

where coefficient $K_{i,j}$ denotes the binary interaction between component i and j and is retrieved from Løvik (2001), whereas coefficients $a_{i,\text{phase}}$ and $b_{i,\text{phase}}$ for a generic pure component i in the phase read:

$$a_{\alpha,\text{phase}} = 0.42748\frac{\left(R_{\text{gas}}T_{\text{critical}}\right)^2}{p_{\text{critical}}}k_\alpha, \tag{C.10}$$
$$b_{\alpha,\text{phase}} = 0.08664\frac{R_{\text{gas}}T_{\text{critical}}}{p_{\text{critical}}}.$$

For water and methanol (condensable components) they read: $K_{H_2O-H_2O}=0$, $K_{CH_3OH-CH_3OH}=0$, $K_{CH_3OH-H_2O}=-0.0789$, whereas k_i reads $\left(1+S\left(1-\sqrt{(T_{\text{reduced},\alpha})}\right)\right)^2$, with $S=s_1+s_2\omega+s_3\omega^2$, $\omega=-\log_{10}\left(p_{\text{pitzer}}/p_{\text{critical}}\right)-1$. The pressure utilized for the evaluation of Pitzer's acentric factor reads

$$p_{\text{pitzer}}(\text{Pa}) = 10^{\left(A+B/T_{\text{pitzer}}+C\log_{10}\left(T_{\text{pitzer}}\right)+DT_{\text{pitzer}}+ET_{\text{pitzer}}^2\right)}\frac{101325}{760} \tag{C.11}$$
$$T_{\text{pitzer}} = 0.7\cdot T_{\text{critical}}.$$

C.3. Source term σ_α in reactor models

The generation of component α in (DE.RWGS.1, DE.METHL.1) and 3 is expressed by the source term σ_α, which reads:

$$\sigma_\alpha = \sum_{k\in K}\nu_{\alpha,k}R_k, \tag{C.12}$$

where the stoichiometric coefficient $\nu_{\alpha,k}$ multiplies the reaction rate of reaction R_k ($mol\,kg_{cat}^{-1}\,s^{-1}$). Reaction rates for RWGS and METHL are reported in the following Sections of this Appendix.

C.4. Reaction rates for reverse water-gas shift reactor (RWGS)

The parameters are selected from Xu and Froment (1989) and reported in Table C.9. The governing kinetic expressions are

$$\text{DEN} = \left(1+K_{CO}p_{CO,\text{bar}}+K_{H_2}p_{H_2,\text{bar}}+K_{CH_4}p_{CH_4,\text{bar}}+K_{H_2O}\frac{x_{H_2O}}{x_{H_2}}\right), \tag{C.13}$$

$$R_{\mathrm{SR}} = 10^3 \frac{k_{\mathrm{SR}}}{p_{\mathrm{H_2,bar}}^{2.5}} \frac{\left(p_{\mathrm{CH_4,bar}} p_{\mathrm{H_2O,bar}} - p_{\mathrm{H_2,bar}}^3 \frac{p_{\mathrm{CO,bar}}}{K_{\mathrm{eq,SR}}}\right)}{\mathrm{DEN}^2},$$

$$R_{\mathrm{WGS}} = 10^3 \frac{k_{\mathrm{WGS}}}{p_{\mathrm{H_2,bar}}} \frac{\left(p_{\mathrm{CO,bar}} p_{\mathrm{H_2O,bar}} - p_{\mathrm{H_2,bar}} \frac{p_{\mathrm{CO_2,bar}}}{K_{\mathrm{eq,WGS}}}\right)}{\mathrm{DEN}^2},$$

$$R_{\mathrm{RMETH}} = 10^3 \frac{k_{\mathrm{RMETH}}}{p_{\mathrm{H_2,bar}}^{3.5}} \frac{\left(p_{\mathrm{CH_4,bar}} p_{\mathrm{H_2O,bar}}^2 - p_{\mathrm{H_2,bar}}^4 \frac{p_{\mathrm{CO_2,bar}}}{K_{\mathrm{eq,RMET}}}\right)}{\mathrm{DEN}^2},$$

where the kinetics parameters k_i and K_j related to reaction and adsorption result from the following Arrhenius-like relations

$$k_i = A(k_i) \exp\left(-\frac{E(k_i)}{R_{\mathrm{gas}} T}\right) \quad \text{and} \quad K_j = A(K_j) \exp\left(-\frac{E(K_j)}{R_{\mathrm{gas}} T}\right). \tag{C.14}$$

Values of coefficients $A(k_i, K_j)$ and $E(k_i, K_j)$ are listed in Table C.9.

C.5. Reaction rates for methanol reactor (METHL)

METHL kinetics are adapted from Graaf et al. (1988) and determined as $\mathrm{mol\,kg_{cat}^{-1}\,s^{-1}}$.

$$\mathrm{DEN} = \left(1 + K_{\mathrm{CO}} f_{\mathrm{CO,bar}} + K_{\mathrm{CO_2}} f_{\mathrm{CO_2,bar}}\right)\left[f_{\mathrm{H_2}}^{0.5} + \left(K_{\mathrm{H_2O}}/K_{\mathrm{H_2}}^{0.5}\right) f_{\mathrm{H_2O}}\right], \tag{C.15}$$

$$R_{\mathrm{CO}\to\mathrm{CH_3OH}} = k_{\mathrm{A3}} K_{\mathrm{CO}} \frac{\left(f_{\mathrm{CO,bar}} f_{\mathrm{H_2,bar}}^{3/2} - \frac{f_{\mathrm{CH_3OH,bar}}}{f_{\mathrm{H_2,bar}}^{0.5} Keq_{\mathrm{CO}\to\mathrm{CH_3OH}}}\right)}{\mathrm{DEN}},$$

$$R_{\mathrm{RWGS}} = k_{\mathrm{B2}} K_{\mathrm{CO_2}} \frac{\left(f_{\mathrm{CO_2,bar}} f_{\mathrm{H_2,bar}} - \frac{f_{\mathrm{H_2O,bar}} f_{\mathrm{CO,bar}}}{Keq_{\mathrm{RWGS}}}\right)}{\mathrm{DEN}},$$

$$R_{\mathrm{CO_2}\to\mathrm{CH_3OH}} = k_{\mathrm{C3}} K_{\mathrm{CO_2}} \frac{\left(f_{\mathrm{CO_2,bar}} f_{\mathrm{H_2,bar}}^{3/2} - \frac{f_{\mathrm{CH_3OH,bar}} f_{\mathrm{H_2O,bar}}}{f_{\mathrm{H_2,bar}}^{1.5} Keq_{\mathrm{CO_2}\to\mathrm{CH_3OH}}}\right)}{\mathrm{DEN}},$$

and

$$k_{\mathrm{A3}} = 2.69 \times 10^7 \exp\left(\frac{-109900}{R_{\mathrm{gas}} T}\right),\ k_{B2} = 7.31 \times 10^8 \exp\left(\frac{-123400}{R_{\mathrm{gas}} T}\right), \tag{C.16}$$

$$k_{\mathrm{C3}} = 4.36 \times 10^2 \exp\left(\frac{-65200}{R_{\mathrm{gas}} T}\right),\ K_{\mathrm{CO}} = 7.99 \times 10^{-7} \exp\left(\frac{58100}{R_{\mathrm{gas}} T}\right),$$

$$K_{\mathrm{CO_2}} = 1.02 \times 10^{-7} \exp\left(\frac{67400}{R_{\mathrm{gas}} T}\right),$$

$$K_{\mathrm{H_2O}} \sqrt{K_{\mathrm{H_2}}} = 4.13 \times 10^{-11} 4 \exp\left(\frac{104500}{R_{\mathrm{gas}} T}\right),$$

$$K_{\mathrm{H_2}} = 1.494 \exp\left(\frac{6025}{R_{\mathrm{gas}} T}\right).$$

Effectiveness factor is set to 1 for both fixed-bed reactors.

C.6. Analytical solution for the compressibility factor in gas phase (METHL)

RKS is adopted for the modeling of the methanol reactor METHL as recommended in the sources, where mixing rules are not implemented (Lewis-Randall approximation: real gases as pure components within a mixture). The reactor operates in gas phase. Therefore, the analytic solution at each discretization point for the compressibility factor $Z_{\alpha\in S, k\in K, \mathrm{gas}}$, where set S includes the components, set K the discretization points, reads:

$$Z_{\alpha,\mathrm{gas},k} = \mathrm{sgn}\left(\Theta_{1,(\alpha,k)}\right) |\Theta_{1,\alpha,k}|^{1/3} + \mathrm{sgn}\left(\Theta_{2,\alpha,k}\right) |\Theta_{2,\alpha,k}|^{1/3} - \frac{\alpha_{\alpha,k}}{3} \tag{C.17}$$

where

$$\Theta_{1,\alpha,k} = -\frac{q_{\alpha,k}}{2} + \sqrt{D_{\alpha,k}} \tag{C.18}$$

$$\Theta_{2,\alpha,k} = -\frac{q_{\alpha,k}}{2} - \sqrt{D_{\alpha,k}}$$

$$D_{\alpha,k} = \frac{q_{\alpha,k}^2}{4} + \frac{p_{\alpha,k}^3}{27}$$

$$q_{\alpha,k} = 2\frac{\alpha_{\alpha,k}^3}{27} - \alpha_{\alpha,k}\frac{\beta_{\alpha,k}}{3} + \gamma_{\alpha,k}$$

$$p_{\alpha,k} = \beta_{\alpha,k} - \frac{\alpha_{\alpha,k}^2}{3}$$

where $\alpha_{\alpha,k}$, $\beta_{\alpha,k}$ and $\gamma_{\alpha,k}$ are calculated as in Appendix C.2 in function of $a_{\alpha,k}$ and $b_{\alpha,k}$ for pure components along the axial coordinate k, therefore without accounting for the mixing rules:

$$A_{\mathrm{EOS},\alpha,\mathrm{k}} = a_{\alpha,\mathrm{k}} \frac{p_k}{\left(R_{\mathrm{gas}} T_k\right)^2}, \tag{C.19}$$

$$B_{\mathrm{EOS},\alpha,\mathrm{k}} = b_{\alpha,\mathrm{k}} \frac{p_k}{\left(R_{\mathrm{gas}} T_k\right)}.$$

Reference is found in Rota (2015).

The fugacity is obtained multiplying the fugacity coefficient with the partial pressure of component i at each discretization point k:

$$f_{\alpha,k} = \Phi_{\alpha,k} p_{\mathrm{tot},k} \zeta_{\alpha,k} \tag{C.20}$$

and the fugacity coefficient $\Phi_{\alpha,k}$ for pure components (Lewis Randall approximation of equal interactions among real components in gas phase) reads:

$$\Phi_{\alpha,k} = 7 \exp\left(Z_{\alpha,\mathrm{gas},k} - 1 - \frac{A_{\mathrm{EOS},\alpha,\mathrm{k}}}{B_{\mathrm{EOS},\alpha,\mathrm{k}}} \log\left(Z_{\alpha,\mathrm{gas},k} + \frac{B_{\mathrm{EOS},\alpha,\mathrm{k}}}{Z_{\alpha,\mathrm{gas},k}}\right) - \log\left(Z_{\alpha,\mathrm{gas},k} - B_{\mathrm{EOS},\alpha,\mathrm{k}}\right)\right). \tag{C.21}$$

Similar to $\alpha_{\alpha,k}$ and $\beta_{\alpha,k}$, $A_{\mathrm{EOS},\alpha,\mathrm{k}}$ and $B_{\mathrm{EOS},\alpha,\mathrm{k}}$ rely on pure component calculations.

C.7. Analytical solution for the compressibility factor in gas phase (COMPR)

The compressibility factor is calculated analytically as shown in Appendix Appendix C.6, with the difference that coefficients α, β, γ are derived accounting for the mixing rules, as in Equation (C.6) in Appendix Appendix C.2.

C.8. Overall heat transfer coefficient U (METHL)

The overall heat transfer coefficient depending on the axial discretization point along the methanol reactor reads

$$U = \left(\frac{1}{\alpha_{\mathrm{eff}}}\right)^{-1}, \tag{C.22}$$

where α_{eff} is the effective heat transfer coefficient. Here, the shell-side heat transfer coefficient is not accounted for. Instead, a constant skin temperature is assumed along the pipe. The definition of α_{eff} for non-adiabatic packed-bed reactors is provided by Martin and Nilles (1993):

$$\frac{1}{\alpha_{\mathrm{eff}}} = \left(\frac{1}{\alpha_{\mathrm{w}}} + \frac{D_{\mathrm{t,METHL}}}{8\Lambda_{\mathrm{r}}}\right). \tag{C.23}$$

Here, α_w and Λ_r, respectively, wall heat transfer coefficient and radial heat conductivity, are retrieved from Bauer and Schlünder (1976) and discussed by Tsotsas (2010) and Martin and Nilles (1993)

$$\alpha_w = \left\{ \left(1.3 + \frac{5}{D_{T,METHL}/D_{cat,METHL}} \right) \frac{\lambda_{bed}}{\lambda_{mix}} + 0.19 \left[\rho_{gas} v \varepsilon \frac{D_{cat,METHL}}{\mu_{mix}} \right]^{0.75} \left[\mu_{mix} \frac{\tilde{C}_{p,gas}}{\lambda_{mix}} \right]^{0.33} \right\} \frac{\lambda_{mix}}{D_{cat,METHL}}, \tag{C.24}$$

$$\Lambda_r = \left\{ \lambda_{bed} + \frac{v \varepsilon C_{tot} \tilde{C}_{p,gas} D_{cat,METHL}}{8 \left[2 - \left(1 - \frac{2}{D_{T,METHL}/D_{cat,METHL}} \right)^2 \right]} \right\}. \tag{C.25}$$

Embedded in the definition of α_w, the heat conductivity across the packed-bed λ_{bed} is defined by the following steps (Tsotsas, 2010):

$$\lambda_{bed} = k_{bed} \lambda_{mix}, \tag{C.26}$$

$$k_{bed} = \left(1 - \sqrt{1-\varepsilon} \right) \varepsilon \left[\left(\varepsilon - 1 + \frac{1}{k_G} \right)^{-1} + k_{rad} \right] + \sqrt{1-\varepsilon} \left(\phi k_p + (1-\phi) k_C \right), \tag{C.27}$$

$$\phi = 0.0077 \quad [-] \quad \text{spheres}, \tag{C.28}$$

$$k_C = \frac{2}{N} \left\{ \frac{B\left(k_p + k_{rad} - 1\right)}{N^2 \cdot k_G \cdot k_P} \log \left(\frac{k_p + k_{rad}}{B\left(k_G + \left(1 - k_G\right) \cdot \left(k_P + k_{rad}\right)\right)} \right) + \frac{B+1}{2B} \left[\frac{k_{rad}}{k_G} - B \left(1 + \frac{1-k_G}{k_G} k_{rad} \right) \right] - \frac{B-1}{N \cdot k_G} \right\}, \tag{C.29}$$

$$k_{rad} = \frac{4 \sigma_{SB}}{2/\varepsilon_E - 1} T^3 \frac{D_{cat,METHL}}{\lambda_{mix}}, \ \sigma_{SB} = 5.67 \cdot 10^{-8} \ [\mathrm{W\,m^{-2}\,K^{-4}}], \ \varepsilon_E = 0.4 \ [-],$$

$$k_G = 1 \ [-], \tag{C.30}$$

$$B = 1.25 \left(\frac{1-\varepsilon}{\varepsilon} \right)^{(10/9)}, \quad \text{and} \quad k_p = \frac{\lambda_{cat}}{\lambda_{mix}}. \tag{C.31}$$

$$N = \frac{1}{k_G} \left(1 + \frac{k_{rad} - B \cdot k_G}{k_p} \right) - B \left(\frac{1}{k_G} - 1 \right) \left(1 + \frac{k_{rad}}{k_p} \right). \tag{C.32}$$

For a thorough description of the single coefficients reported above, see sources.

C.9. Interstitial velocity for tubular reactors (METHL and RWGS)

The interstitial velocity profile is derived in fulfillment of the total mass balance between inlet and current section of the reactor tube. At a given section along the reactor tube, interstitial velocity reads:

$$v = \frac{\sum_{\alpha \in S} \left(\dot{N}_{in,\alpha} M_\alpha \right)}{C_{gas} A_{cross} \varepsilon \sum_{\alpha \in S} \left(\zeta_\alpha M_\alpha \right)}, \tag{C.33}$$

where $\dot{N}_{0,\alpha}$ is the feed flowrate of component α and M_α its molecular weight, C_{tot} is the total concentration at the current reactor section defined as in Equation (5), A_{cross} is the cross sectional area without voids, ε the void fraction, ζ_α the mole fraction at the point.

C.10. Derivation of the component mass balances in molar formulation (METHL and RWGS)

The molar formulation of the material balances for the single components (DE.RWGS.1 and DE.METHL.1), is obtained from the incorporation of the total mass balance in molar form in the component mass balances.

The total mass balance (moles per second in the cross sectional volume of reactor) reads:

$$v \varepsilon \frac{dC_{tot}}{dz} = (1-\varepsilon) \rho_{cat} \sum_\alpha \sigma_\alpha, \tag{C.34}$$

and is substituted in the component mole balance, which is derived as:

$$v \varepsilon \frac{d\zeta_\alpha}{dz} = (1-\varepsilon) \rho_{cat} \sigma_\alpha, \tag{C.35}$$

$$v \varepsilon \left(C_{tot} \frac{\partial \zeta_\alpha}{\partial z} + \zeta_\alpha \frac{\partial C_{tot}}{\partial z} \right) = (1-\varepsilon) \rho_{cat} \sigma_\alpha, \tag{C.36}$$

$$\left(v \varepsilon C_{tot} \frac{d\zeta_\alpha}{dz} + (1-\varepsilon) \rho_{cat} \zeta_\alpha \sum_\alpha \sigma_\alpha \right) = (1-\varepsilon) \rho_{cat} \sigma_\alpha. \tag{C.37}$$

This allows to remove the partial derivative of the total concentration in space from the material balance.

Appendix D. Supplementary section - cost functions

CEPCI cost indices have been retrieved. They are used to actualize the original cost functions. For 1968, 1987, 2013 and 2022 they are 113.6, 323.8, 567.3 and 906.3, respectively. Sources are found on websites (Baasel, 1990; CEPCI Cost Indices, 2022). Lifetimes for units and components are reported in Table 5. For hydrogen compressor, a lifetime of 10 years is assumed.

D.1. Tubular reactors

The correlation for tubular bundle reactors (METHL) is the same for shell and tubes heat exchangers and is retrieved from Peters et al. (2003). It reads:

$$C_{METHL,vessel,\$} = 4.9 \times 10^3 \left(0.10764 \cdot A_{METHL,tot} \right)^{0.68} 1.61 \left(2.7 + \left(\frac{2.7}{100} \right)^{0.07} \right) \left(\frac{CEPCI_{2022}}{CEPCI_{1987}} \right), \tag{D.1}$$

and is defined for stainless steel shell and tubes heat exchangers; $A_{METHL,tot}$ is the total area of exchange, from tubes to reactor coolant. The formula is adapted from a graphical diagram, and converted to use SI units of measurement.

The adiabatic RWGS stage is given by Douglas (1988) and reads:

$$C_{RWGS,vessel,\$} = 101.9 \left(3.28084 \cdot D_{t,RWGS} \right)^{1.066} \left(3.28084 L_{t,RWGS} \right)^{0.802} (2.18 + 1) \left(\frac{CEPCI_{2022}}{CEPCI_{1968}} \right), \tag{D.2}$$

defined for carbon steel at low pressure. Both, Equation (D.1) and (D.2), are expressed in Dollar, which is converted to Euro according to the prevailing change at the time of the computations 1 €/1.05 $. Similarly for all prices adopted in the Contribution.

For RWGS, a standard industrial nickel catalyst on alumina support has been selected. Its estimated cost: $13\,\$\,kg^{-1}$. For the methanol reactor catalyst a price of $45\,\$\,kg^{-1}$ is assumed. Both references are averaged values from online sources (MS-2 methanol catalyst, 2022; Nickel alumina catalyst for hydrogenation, 2022).

D.2. SOEC

In absence of a reliable cost per unit of SOEC area, a cost per unit of power input is adopted: $0.1253\,€\,W^{-1}$ (Anghilante et al., 2018).

D.3. Compressor

The hydrogen compressor installation cost is retrieved from a graphical diagram in Peters et al. (2003):

$$C_{CPR,H_2,\$} = 21.0 \times 10^3 \left(\frac{\dot{W}_{CPR}}{29840}\right)^{0.8} \left(\frac{CEPCI_{2022}}{CEPCI_{1987}}\right) 1.49. \quad (D.3)$$

References

Mucci, S., Mitsos, A., Bongartz, D., 2023. Power-to-x processes based on PEM water electrolyzers: a review of process integration and flexible operation. Comput. Chem. Eng., 108260. https://doi.org/10.1016/j.compchemeng.2023.108260.

Bruns, B., Herrmann, F., Polyakova, M., Grünewald, M., Riese, J., 2020. A systematic approach to define flexibility in chemical engineering. J. Adv. Manuf. Process. 2 (4), e10063. https://doi.org/10.1002/amp2.10063.

Grossmann, I.E., Sargent, R.W.H., 1978. Optimum design of chemical plants with uncertain parameters. AIChE J. 24 (6), 1021–1028. https://doi.org/10.1002/aic.690240612.

Iyer, R., Grossmann, I.E., 1998. Synthesis and operational planning of utility systems for multiperiod operation. Comput. Chem. Eng. 22 (7–8), 979–993. https://doi.org/10.1016/S0098-1354(97)00270-6.

Martín, M., 2016. Methodology for solar and wind energy chemical storage facilities design under uncertainty: methanol production from CO2 and hydrogen. Comput. Chem. Eng. 92, 43–54. https://doi.org/10.1016/j.compchemeng.2016.05.001.

Peng, X., Root, T.W., Maravelias, C.T., 2019. Optimization-based process synthesis under seasonal and daily variability: application to concentrating solar power. AIChE J. 65 (7), e16458. https://doi.org/10.1002/aic.16458.

Short, M., Isafiade, A.J., Fraser, D.M., Kravanja, Z., 2016. Two-step hybrid approach for the synthesis of multi-period heat exchanger networks with detailed exchanger design. Appl. Therm. Eng. 105, 807–821. https://doi.org/10.1016/j.applthermaleng.2016.05.065.

Herrmann, F., Grünewald, M., Riese, J., 2020. Flexibility of power-to-gas plants: a case study. Chem. Ing. Tech. 92 (12), 1983–1991. https://doi.org/10.1002/cite.202000063.

Chen, C., Yang, A., 2021. Power-to-methanol: the role of process flexibility in the integration of variable renewable energy into chemical production. Energy Convers. Manag. 228, 113673. https://doi.org/10.1016/j.enconman.2020.113673.

Zimmermann, R.T., Bremer, J., Sundmacher, K., 2022. Load-flexible fixed-bed reactors by multi-period design optimization. Chem. Eng. J. 428, 130771. https://doi.org/10.1016/j.cej.2021.130771.

Burre, J., Bongartz, D., Brée, L., Roh, K., Mitsos, A., 2020. Power-to-x: between electricity storage, e-production, and demand side management. Chem. Ing. Tech. 92 (1–2), 74–84. https://doi.org/10.1002/cite.201900102.

Zhang, Q., Grossmann, I.E., 2016. Enterprise-wide optimization for industrial demand side management: fundamentals, advances, and perspectives. Chem. Eng. Res. Des. 116, 114–131. https://doi.org/10.1016/j.cherd.2016.10.006.

Dieterich, V., Buttler, A., Hanel, A., Spliethoff, H., Fendt, S., 2020. Power-to-liquid via synthesis of methanol, dme or Fischer–tropsch-fuels: a review. Energy Environ. Sci. 13 (10), 3207–3252. https://doi.org/10.1039/D0EE01187H.

Prabhakaran, P., Graf, F., Koeppel, W., Kolb, T., 2023. Modelling and validation of energy systems with dynamically operated power to gas plants for gas-based sector coupling in de-central energy hubs. Energy Convers. Manag. 276, 116534. https://doi.org/10.1016/j.enconman.2022.116534.

Kreitz, B., Brauns, J., Wehinger, G.D., Turek, T., 2020. Modeling the dynamic power-to-gas process: coupling electrolysis with CO2 methanation. Chem. Ing. Tech. 92 (12), 1992–1997. https://doi.org/10.1002/cite.202000019.

Moioli, E., 2022. Process intensification and energy transition: a necessary coupling? Chem. Eng. Process. 179, 109097. https://doi.org/10.1016/j.cep.2022.109097.

Riaz, A., Zahedi, G., Klemeš, J.J., 2013. A review of cleaner production methods for the manufacture of methanol. J. Clean. Prod. 57, 19–37. https://doi.org/10.1016/j.jclepro.2013.06.017.

Verhelst, S., Turner, J.W., Sileghem, L., Vancoillie, J., 2019. Methanol as a fuel for internal combustion engines. Prog. Energy Combust. Sci. 70, 43–88. https://doi.org/10.1016/j.pecs.2018.10.001.

Buttler, A., Spliethoff, H., 2018. Current status of water electrolysis for energy storage, grid balancing and sector coupling via power-to-gas and power-to-liquids: a review. Renew. Sustain. Energy Rev. 82, 2440–2454. https://doi.org/10.1016/j.rser.2017.09.003.

Simoes, S.G., Catarino, J., Picado, A., Lopes, T.F., Di Berardino, S., Amorim, F., Girio, F., Rangel, C., de Leao, T.P., 2021. Water availability and water usage solutions for electrolysis in hydrogen production. J. Clean. Prod. 315, 128124. https://doi.org/10.1016/j.jclepro.2021.128124.

Ghobeity, A., Mitsos, A., 2010. Optimal time-dependent operation of seawater reverse osmosis. Desalination 263 (1–3), 76–88. https://doi.org/10.1016/j.desal.2010.06.041.

Bui, M., Adjiman, C.S., Bardow, A., Anthony, E.J., Boston, A., Brown, S., Fennell, P.S., Fuss, S., Galindo, A., Hackett, L.A., et al., 2018. Carbon capture and storage (CCS): the way forward. Energy Environ. Sci. 11 (5), 1062–1176. https://doi.org/10.1039/C7EE02342A.

Wang, X., Song, C., 2020. Carbon capture from flue gas and the atmosphere: a perspective. In: Frontiers in Energy Research, vol. 8, 560849.

Li, K., Cousins, A., Yu, H., Feron, P., Tade, M., Luo, W., Chen, J., 2016. Systematic study of aqueous monoethanolamine-based CO2 capture process: model development and process improvement. Energy Sci. Eng. 4 (1), 23–39. https://doi.org/10.1002/ese3.101.

Knudsen, J.N., Jensen, J.N., Vilhelmsen, P.-J., Biede, O., 2009. Experience with CO2 capture from coal flue gas in pilot-scale: testing of different amine solvents. Energy Proc. 1 (1), 783–790. https://doi.org/10.1016/j.egypro.2009.01.104.

Ozkan, M., Nayak, S.P., Ruiz, A.D., Jiang, W., 2022. Current status and pillars of direct air capture technologies. iScience, 103990. https://doi.org/10.1016/j.isci.2022.103990.

IEA, 2022. Energy needs of DACS and DAC with CO2 use by technology and CO2 destination. https://www.iea.org/data-and-statistics/charts.

Gualtieri, G., Secci, S., 2012. Methods to extrapolate wind resource to the turbine hub height based on power law: a 1-h wind speed vs. Weibull distribution extrapolation comparison. Renew. Energy 43, 183–200. https://doi.org/10.1016/j.renene.2011.12.022.

Graaf, G.H., 1986. Chemical equilibria in methanol synthesis. Chem. Eng. Sci. 41 (11), 2883–2890. https://doi.org/10.1016/0009-2509(86)80019-7.

Udagawa, J., Aguiar, P., Brandon, N., 2007. Hydrogen production through steam electrolysis: model-based steady state performance of a cathode-supported intermediate temperature solid oxide electrolysis cell. J. Power Sources 166 (1), 127–136. https://doi.org/10.1016/j.jpowsour.2006.12.081.

Petipas, F., Brisse, A., Bouallou, C., 2013. Model-based behaviour of a high temperature electrolyser system operated at various loads. J. Power Sources 239, 584–595. https://doi.org/10.1016/j.jpowsour.2013.03.027.

Bremer, J., Sundmacher, K., 2019. Operation range extension via hot-spot control for catalytic CO2 methanation reactors. React. Chem. Eng. 4 (6), 1019–1037. https://doi.org/10.1039/c9re00147f.

Seidel, C., Jörke, A., Vollbrecht, B., Seidel-Morgenstern, A., Kienle, A., 2018. Kinetic modeling of methanol synthesis from renewable resources. Chem. Eng. Sci. 175, 130–138. https://doi.org/10.1016/j.ces.2017.09.043.

Graaf, G.H., Stamhuis, E.J., Beenackers, A.A.C.M., 1988. Kinetics of low-pressure methanol synthesis. Chem. Eng. Sci. 43 (12), 3185–3195. https://doi.org/10.1016/0009-2509(88)85127-3.

Xu, J., Froment, G.F., 1989. Methane steam reforming, methanation and water-gas shift: I. Intrinsic kinetics. AIChE J. 35 (1), 88–96. https://doi.org/10.1002/aic.690350109.

Lüdtke, K.H., 2004. Process Centrifugal Compressors: Basics, Function, Operation, Design, Application. Springer Science & Business Media.

Nederstigt, P., Pecnik, R., 2023. Generalised isentropic relations in thermodynamics. Energies 16 (5), 2281.

Wächter, A., Biegler, L.T., 2006. On the implementation of an interior-point filter line-search algorithm for large-scale nonlinear programming. Math. Program. 106 (1), 25–57. https://doi.org/10.1007/s10107-004-0559-y.

Andersson, J., 2013. A general-purpose software framework for dynamic optimization (Een algemene softwareomgeving voor dynamische optimalisatie). PhD dissertation. KU Leuven.

Andersson, J.A., Gillis, J., Horn, G., Rawlings, J.B., Diehl, M., 2019. CasADi: a software framework for nonlinear optimization and optimal control. Math. Program. Comput. 11 (1), 1–36. https://doi.org/10.1007/s12532-018-0139-4.

HSL, 2007. A collection of fortran codes for large scale scientific computation. https://www.hsl.rl.ac.uk/catalogue/.

Methanol Price Trend and Forecast, 2022. https://www.chemanalyst.com/Pricing-data/methanol-1. (Accessed 7 October 2022).

Anghilante, R., Colomar, D., Brisse, A., Marrony, M., 2018. Bottom-up cost evaluation of SOEC systems in the range of 10–100 MW. Int. J. Hydrog. Energy 43 (45), 20309–20322. https://doi.org/10.1016/j.ijhydene.2018.08.161.

Zakeri, B., Syri, S., 2015. Electrical energy storage systems: a comparative life cycle cost analysis. Renew. Sustain. Energy Rev. 42, 569–596. https://doi.org/10.1016/j.rser.2014.10.011.

Hydrogen storage cost analysis final public report. U.S. Department of Energy. https://www.osti.gov/servlets/purl/1082754. (Accessed 27 July 2022).

GmbH, S.E., 2012. Sulzon s95-2.1 mw. Wind turbine generator technical specification. https://environment.govmu.org/Documents/eia/eiareports/suzlon_windfarm/annex8.pdf.

Das Wetter das ganze Jahr über an einem beliebigen Ort der Erde (Weather Spark). https://de.weatherspark.com/y/71338/Durchschnittswetter-in-Magdeburg-Deutschland-das-ganze-Jahr. (Accessed 5 August 2022).

Løvik, I., 2001. Modelling, estimation and optimization of the methanol synthesis with catalyst deactivation. PhD dissertation. NTNU, Department of Chemical Engineering.

Rota, R., 2015. Fondamenti di Termodinamica Dell'ingegneria Chimica. Pitagora Editore.

Martin, H., Nilles, M., 1993. Radiale Wärmeleitung in durchströmten Schüttungsrohren. Chem. Ing. Tech. 65 (12), 1468–1477. https://doi.org/10.1002/cite.330651206.

Bauer, R., Schlünder, E.U., 1976. Effektive radiale Wärmeleitfähigkeit gasdurchströmter Schüttungen aus Partikeln unterschiedlicher Form. Chem. Ing. Tech. 48 (3), 227–228. https://doi.org/10.1002/cite.330480309.

Tsotsas, E., 2010. M7 heat and mass transfer in packed beds with fluid flow. In: VDI Heat Atlas. Springer Berlin Heidelberg, pp. 1327–1342.

Baasel, W.D., 1990. Preliminary Chemical Engineering Plant Design, vol. 2. Van Nostrand Reinhold, New York.

CEPCI Cost Indices, 2022. https://www.toweringskills.com/financial-analysis/cost-indices/. (Accessed 16 May 2022).
Peters, M.S., Timmerhaus, K.D., West, R.E., et al., 2003. Plant Design and Economics for Chemical Engineers, vol. 3. McGraw-Hill, New York.
Douglas, J.M., 1988. Conceptual Design of Chemical Processes. McGraw-Hill, New York.
MS-2 methanol catalyst. https://www.alibaba.com/product-detail/MS-2-Methanol-catalyst_1600191862387.html. (Accessed 18 July 2022).
Nickel alumina catalyst for hydrogenation. https://www.alibaba.com/product-detail/Nickel-Alumina-Catalyst-Factory-Price-For_62039092901.html. (Accessed 18 July 2022).